



Variation of plagioclase shape with size in intermediate magmas: a window into incipient plagioclase crystallisation

Martin F. Mangler¹ · Madeleine C. S. Humphreys¹ · Fabian B. Wadsworth¹ · Alexander A. Iveson¹ · Michael D. Higgins²

Received: 21 December 2021 / Accepted: 16 May 2022 / Published online: 22 June 2022
© The Author(s) 2022

Abstract

Volcanic rocks commonly display complex textures acquired both in the magma reservoir and during ascent to the surface. While variations in mineral compositions, sizes and number densities are routinely analysed to reconstruct pre-eruptive magmatic histories, crystal shapes are often assumed to be constant, despite experimental evidence for the sensitivity of crystal habit to magmatic conditions. Here, we develop a new program (*ShapeCalc*) to calculate 3D shapes from 2D crystal intersection data and apply it to study variations of crystal shape with size for plagioclase microlites ($l < 100 \mu\text{m}$) in intermediate volcanic rocks. The smallest crystals tend to exhibit prismatic 3D shapes, whereas larger crystals ($l > 5\text{--}10 \mu\text{m}$) show progressively more tabular habits. Crystal growth modelling and experimental constraints indicate that this trend reflects shape evolution during plagioclase growth, with initial growth as prismatic rods and subsequent preferential overgrowth of the intermediate dimension to form tabular shapes. Because overgrowth of very small crystals can strongly affect the external morphology, plagioclase microlite shapes are dependent on the available growth volume per crystal, which decreases during decompression-driven crystallisation as crystal number density increases. Our proposed growth model suggests that the range of crystal shapes developed in a magma is controlled by the *temporal evolution* of undercooling and total crystal numbers, i.e., distinct cooling/decompression paths. For example, in cases of slow to moderate magma ascent rates and quasi-continuous nucleation, early-formed crystals grow larger and develop tabular shapes, whereas late-stage nucleation produces smaller, prismatic crystals. In contrast, rapid magma ascent may suppress nucleation entirely or, if stalled at shallow depth, may produce a single nucleation burst associated with tabular crystal shapes. Such variation in crystal shapes have diagnostic value and are also an important factor to consider when constructing CSDs and models involving magma rheology.

Keywords Crystal growth · 3D crystal shape · Stereology · Plagioclase crystallisation · Nucleation · ShapeCalc

Introduction

Crystal shape has long been known to reflect magmatic conditions during their growth (cf. reviews by Kostov and Kostov 1999; Higgins 2006). For example, magma undercooling ΔT (i.e., supersaturation of the magma in response to cooling or decompression) dictates whether crystal growth

rates are controlled by diffusion (large $\Delta T \gtrsim 80^\circ\text{C}$) or interface kinetics (relatively smaller ΔT), and in the latter case it may also impose a specific growth mechanism (i.e., continuous growth, surface nucleation or screw dislocation) (Kirkpatrick 1975; Dowty 1980; Muncill and Lasaga 1987, 1988; Cabane et al. 2005). Undercooling-driven variations in rate-controlling processes and growth mechanisms generate changes in crystal shapes, with diffusion-controlled growth producing hopper, skeletal and dendritic morphologies, while interface-controlled growth forms euhedral crystals (Lofgren 1974; Kirkpatrick et al. 1979; Muncill and Lasaga 1987). Over decades of cooling (e.g., Lofgren et al. 1974; Walker et al. 1976; Nabelek et al. 1978; Muncill and Lasaga 1988; Watanabe and Kitamura 1992; Duchêne et al. 2008; Pupier et al. 2008; Iezzi et al. 2011; Giuliani et al. 2020) and decompression experiments (e.g., Geschwind

Communicated by Timothy L. Grove.

✉ Martin F. Mangler
martin.mangler@durham.ac.uk

¹ Department of Earth Sciences, Durham University, Durham DH1 3LE, UK

² Sciences Appliquées, Université du Québec À Chicoutimi, Chicoutimi, Québec G7H2B1, Canada

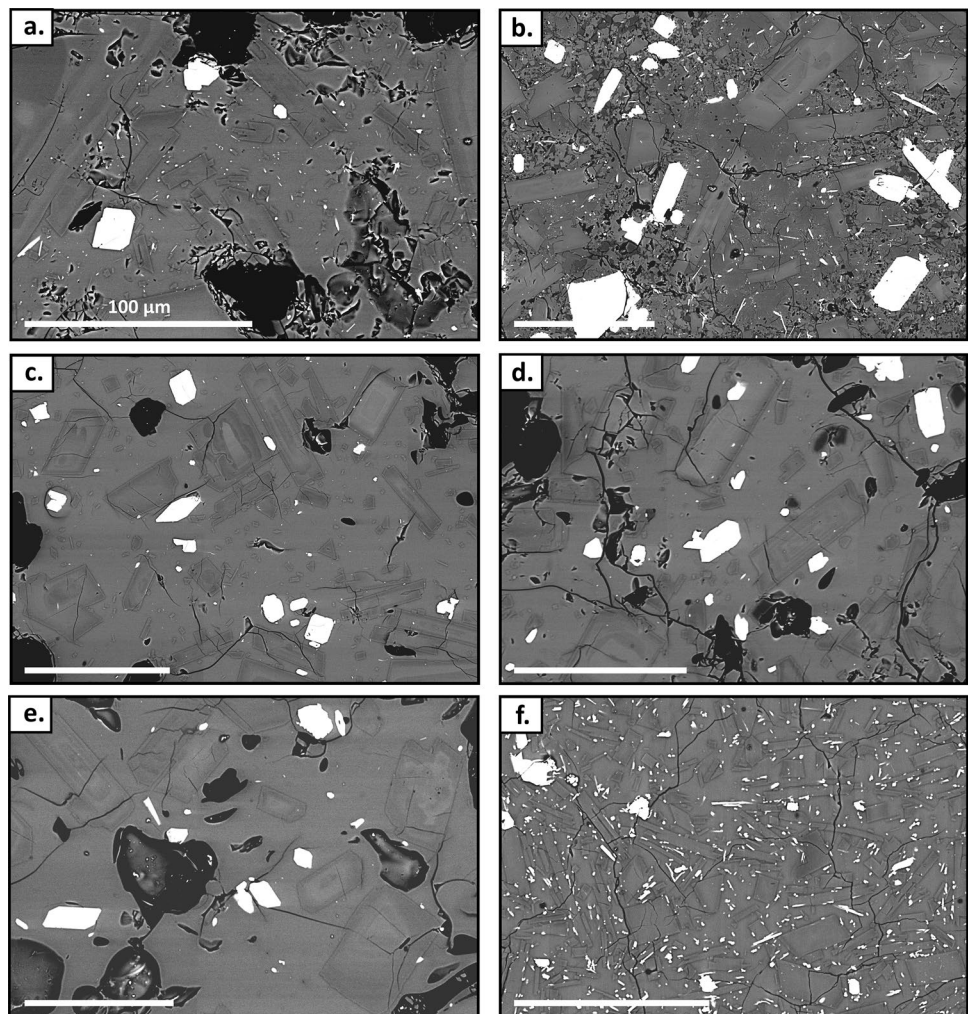
and Rutherford 1995; Hammer and Rutherford 2002; Couch et al. 2003; Martel and Schmidt 2003; Brugger and Hammer 2010; Martel 2012; Mollard et al. 2012; Shea and Hammer 2013; Riker et al. 2015; Befus and Andrews 2018) in basaltic and silicic systems, a general view has emerged that low magma undercoolings produce equant crystal shapes, and that increasing undercooling leads to more tabular shapes. In addition, Higgins and Chandrasekharam (2007) suggested that crystal shape can be modified by shearing or stirring.

On the other hand, it is also well known that many erupted magmas show crystals ranging from sub- μm to cm in size, a feature which is commonly exploited in crystal size distribution (CSD) analysis to infer magma ascent pathways, crystallisation kinetics, or crystal residence times (Marsh 1988; Cashman and Marsh 1988; Cashman 2020). Multiple crystal populations in a magma suggest multiple nucleation and growth events under changing magmatic conditions (e.g., magma undercooling). For example, microlite populations may form by decompression during ascent to the surface or by cooling during lava emplacement. It is therefore reasonable to assume that each crystal population

will develop distinct crystal morphologies reflecting these changing magmatic conditions. Indeed, large variations in 3D crystal shapes have been reported within both experimental runs (Duchêne et al. 2008) and natural samples (Cashman and McConnell 2005; Mock and Jerram 2005), and contrasting 2D shapes for microlites of different sizes are visually discernible in many intermediate magmas (e.g., Hammer et al. 1999; Preece et al. 2016; Bain et al. 2019; Wallace et al. 2020; Fig. 1). Nonetheless, CSDs are generally constructed with the assumption that all crystal sizes have the same shape.

The scope of this paper is twofold. Firstly, we present a new stereological conversion program to estimate 3D crystal shapes from 2D width-length data: *ShapeCalc* covers a larger number and range of potential crystal shapes than existing software, and it offers robust constraints on the uncertainties associated with 3D shape estimates. Secondly, we study variations in 3D crystal shape with size for plagioclase microlites ($l < 100 \mu\text{m}$) in natural magmas of intermediate composition. We quantify how crystal shape changes with size and use the results to constrain how plagioclase

Fig. 1 Backscattered electron images of samples analysed in this study. (a–e) Mt. St. Helens. (a) SH52-2 (Dec 1980), (b) MSH90-9 (1982), (c) SH131A-2 (Aug 1982), (d) SH157 (Jun 1984), (e) SH226 (Oct 1986). (f) Santiaguito, SG-09-04 (2000). Note the differences in numbers, sizes and shapes of plagioclase crystals (the low contrast mineral phase)



growth under changing magmatic conditions shapes crystal morphologies.

Samples, data acquisition and nomenclature

Samples and data acquisition

Textural data for crystal size and shape analysis was acquired for five dome rocks spanning the 1980–86 Mt. St. Helens eruption and two lava samples from the 1986–89 and 2000 eruptions of Santiaguito (Table 1, Fig. 1). All samples have previously been described in detail (Cooper et al. 2008; Streck et al. 2008; Scott et al. 2012; 2013). In addition, we re-analysed published textural data for microlites in dome rocks and pumice from Galeras (Bain et al. 2019; 2021). Plagioclase microlites in all samples are faceted and euhedral with no significant evidence for disequilibrium (e.g., skeletal) growth.

For Mt. St. Helens and Santiaguito lavas, we used one thin section per sample to acquire back-scattered electron (BSE) maps of the crystalline groundmass on a Hitachi SU-70 field emission scanning electron microscope at Durham University (UK), using 15 kV accelerating voltage, 15 mm working distance, 60 μs dwell time, and 500–1000 \times magnification. Crystal sizes captured typically range from 1 to 100 μm length, with minimal and maximal crystal lengths constrained by the image resolution and map size, respectively. Three to 14 stitched BSE maps $\leq 1 \text{ mm}^2$ were acquired per sample to ensure a sufficient number of plagioclase crystals for shape analysis across all crystal lengths ($n_{\text{sample}} \approx 600\text{--}2500$).

For each map, widths (w) and lengths (l) of all plagioclase crystal intersections not touching the edges were measured using line measurements in image processing program ImageJ (Schneider et al. 2012). This method is different from the common approach of obtaining w and l from an ellipse with the same area, orientation and centroid as the crystal intersection (e.g., Higgins 2000). The best-fit ellipse approximation is time-efficient as it can be semi-automated using image processing software (e.g., Lormand et al. 2018). However, it requires full outlines to be specified for each crystal, which can be challenging for intergrown crystals and may introduce random errors if crystal outlines have to be estimated. We tested the consistency of the two methods by measuring and processing ~ 600 crystals using both crystal outlines and direct line measurements (Online Resource 4). Resulting shape data are in good agreement, suggesting that the best-fit ellipse approach does indeed yield robust crystal w - l data that are directly comparable to data derived from direct line measurements. Direct measurements of l and w were used in this study nonetheless as they are judged to

be conceptually more robust in the presence of contiguous crystals.

Binning strategy

Width-length datasets for each sample were subdivided by crystal length into fractions of $l=0\text{--}5 \mu\text{m}$, $5\text{--}10 \mu\text{m}$, $10\text{--}30 \mu\text{m}$, and $30\text{--}100 \mu\text{m}$ to test for variations in 3D shape with crystal size. The chosen bin limits are somewhat arbitrary but ensure sufficient crystal intersection data for robust 3D shape modelling in each bin ($n_{\text{min}} \approx 100\text{--}200$, depending on crystal shape; Online Resource 4), and their consistent use facilitates direct comparisons between samples.

2D to 3D shape conversion: *ShapeCalc*

Crystal intersections are 2D representations of 3D objects, and 2D intersection sizes and shapes (approximated by w and l) are not a straightforward measure of 3D short, intermediate, and long crystal dimensions ($S:I:L$; e.g., Higgins 1994; 2000). Constraining true 3D shapes requires a robust statistic of 2D w - l measurements as well as knowledge of the size(s) and orientation of crystals (preferred vs. random). Higgins (1994) showed that for a population of randomly oriented, anisotropic 3D objects of same size and shape, the most likely intersection length l is close to the 3D intermediate dimension I , and the most likely intersection width w approximates the 3D short dimension S . Hence, the mode of a 2D w/l distribution yields the 3D $S:I$ ratio of the true shape (Higgins 1994; 2000). Estimates of the long dimension L are more difficult to obtain and less robust, as sections along the elongate axis are rare. Higgins (1994; 2000) proposed an estimation of I/L based on the skewness of the w/l distribution.

Higgins' equations relating 2D w/l to 3D $S:I:L$ are based on numerical models in which a rectangular block with a defined $S:I:L$ is randomly sectioned 50,000 times to produce a representative w/l distribution for the known 3D shape (Higgins 1994). A version of this numerical model using 20,000 random sections is included in the crystal size distribution program *CSDCorrections* (Higgins 2000). In *CSDCorrections*, the user is required to input estimates for $S:I:L$, which are used to generate a model w/l distribution. The primary purpose of the model distributions is to perform tailing corrections during the calculation of CSDs, but *CSDcorrections* also provides a visual comparison of model and sample w/l distributions to check the adequacy of the input $S:I:L$.

A similar numerical modelling approach is used by the standalone program *CSDslice* (Morgan and Jerram 2006). Here, the w/l model distributions are based on 10,000 random intersections, which are obtained by rotating a model crystal into random orientations and cutting it perpendicular

to the z-axis of a reference coordinate system. *CSDslice* automatically compares sample w/l distributions with its database of 703 model w/l distributions for 3D shapes from 1:1:1 to 1:10:10 and identifies the five best $S:I:L$ estimates based on a goodness of fit test centred on the mode of the distribution. Best $S:I:L$ estimates from *CSDslice* are commonly used as input for *CSDCorrections* (e.g., Salisbury et al. 2008; Brugger and Hammer 2010; Bain et al. 2019; Lormand et al. 2020).

The respective model w/l distributions used by *CSDCorrections* and *CSDslice* are consistent for shapes with $S/I \ll 1$, where the modes of the w/l distributions reflect S/I (Fig. 2a, b). However, significant differences in model w/l distributions are observed for shapes with $S/I \approx 1$ (i.e., equant and prismatic shapes; Fig. 2c). In particular, while *CSDCorrections* w/l distributions show a mode of $w/l = 1$ reflecting $S \approx I$, *CSDslice* data lack a clear mode. This indicates that there may be an error in the algorithm used by *CSDslice* that is most evident for prismatic shapes. The lack of a clear mode renders *CSDslice* model w/l distributions non-unique. For example, *CSDslice* model w/l distributions for multiple different shapes can be combined to

closely reproduce its 1:1:10 model distribution ($R^2_{CSDslice} > 0.8$) (Fig. 2d). This suggests that the model distributions underpinning *CSDslice* tend to return a shape with $S \sim I$ (i.e., 1:1:L) for sample w/l distributions without a clear modal peak. Natural w/l distributions derived from igneous rocks often lack such clear modes due to the presence of multiple crystal populations as well as some variability in shape within a single population (e.g., Duchêne et al. 2008). We therefore speculate that many natural samples are likely to produce a 1:1:L outcome using *CSDslice*, irrespective of their true crystal shapes. Indeed, published plagioclase microlite shape estimates derived by *CSDslice* are dominated by shapes with $S \approx I$ (e.g., $S:I = 1:1.1$ – $1:1.5$ in Preece et al. 2013, 2016; Bain et al. 2019; and Wallace et al. 2020). Furthermore, a core limitation of *CSDslice* is that its model database is limited to 3D shapes from 1:1:1 to 1:10:10, and natural crystal shapes with higher $S:I$ or $S:L$ can therefore not be reproduced. In our experience, this can generate artefacts suggesting a prevalence of 1:10:10 shapes, particularly for experimental samples, where shapes with $S:L \approx 1:20$ have been reported (Muncill

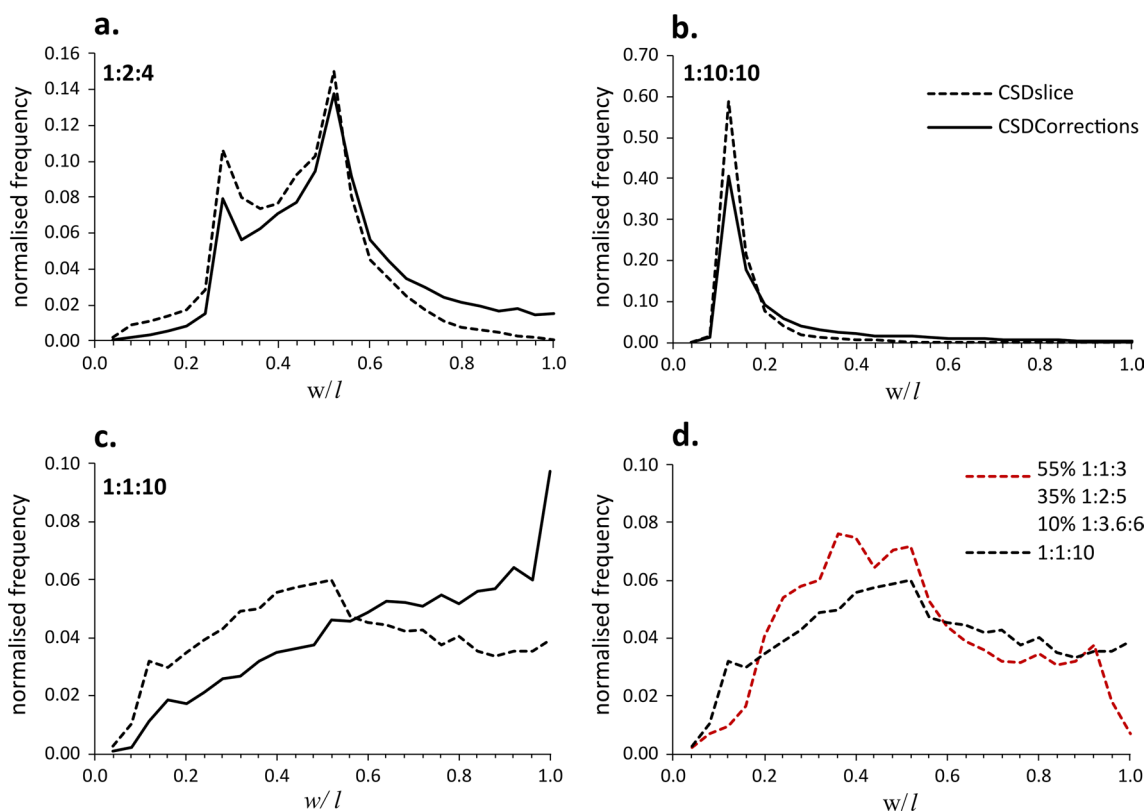


Fig. 2 (a–c) Comparison of model 2D w/l distributions used by *CSDslice* (Morgan and Jerram 2006; dotted lines) and *CSDCorrections* (Higgins 2000; solid lines). Each distribution is obtained by 10,000 (*CSDslice*) or 20,000 (*CSDCorrections*) random sections of a model crystal shape. (a) 1:2:4, (b) 1:10:10, (c) 1:1:10. Note the large dis-

crepancies for 1:1:10 model shapes. (d) Mixing of three *CSDslice* model populations shows good agreement with its 1:1:10 model distribution ($R^2_{CSDslice} > 0.8$), illustrating how may yield erroneous 3D shape estimates if multiple crystal populations with varying shapes are present in a sample

and Lasaga 1988; Hammer and Rutherford 2002). Finally, in light of the significant differences in model w/l distributions between *CSDslice* and *CSDCorrections* (Fig. 2), we suggest that it would be more internally consistent to use the same w/l model distributions for both 3D shape estimates and tailing corrections of CSDs.

With these considerations in mind, we created *ShapeCalc*, a program implemented in Microsoft® Excel that automatically compares a sample w/l distribution with 2618 model w/l distributions generated using *CSDCorrections*, covering an expanded range of shapes from 1:1:1 to 1:20:20 (Online Resources 1 and 2). The best match between sample and model distributions is found by maximising the cumulative measure of the goodness of fit (termed R_c^2 , Online Resource 2). Here, we only report models with $R_c^2 > 0.975$, as lower values indicate unsatisfactory model fits (Figure S2), though the model will still generate outputs at lower R_c^2 that the individual user can evaluate. Uncertainties on the best shape estimate are given as 1SD (standard deviation) of the 300 best model fits, which may reflect natural shape variability in monodisperse crystal populations as well as statistical limitations on S/I and I/L . An example output produced by *ShapeCalc* is shown in Fig. 3, and the program and its full documentation are provided in Online Resources 1 and 2.

Data presentation and shape nomenclature

We present 3D shape data using Zingg diagrams (after Zingg 1935), which plot the 3D intermediate to long axis ratio I/L against the 3D short to intermediate axis S/I (Fig. 4a). Throughout this work, we refer to 3D shapes with $S \approx I \approx L$ (e.g., 1:1:1) as *equant*; shapes with $S \approx I < L$ (e.g., 1:1:10) as *prismatic* or *rods*; shapes with $S < I \approx L$ (e.g., 1:10:10) as *tabular*; and shapes with $S < I < L$ (e.g., 1:10:100) as *bladed*. Shapes with low S/I are most likely to show *elongate* 2D intersections, whereas shapes with high S/I tend to exhibit *square* intersections (Fig. 4a). We note that the term *acicular* technically refers to 3D needle shapes (i.e., $S \approx I \ll L$), and the term should not be used to describe elongate 2D intersections, as these are related to tabular or bladed 3D crystal shapes.

Results

For binned datasets, *ShapeCalc* results for Mt. St. Helens, Santiaguito and Galeras show a consistent decrease in S/I with increasing crystal size (Table 1, Fig. 4): the

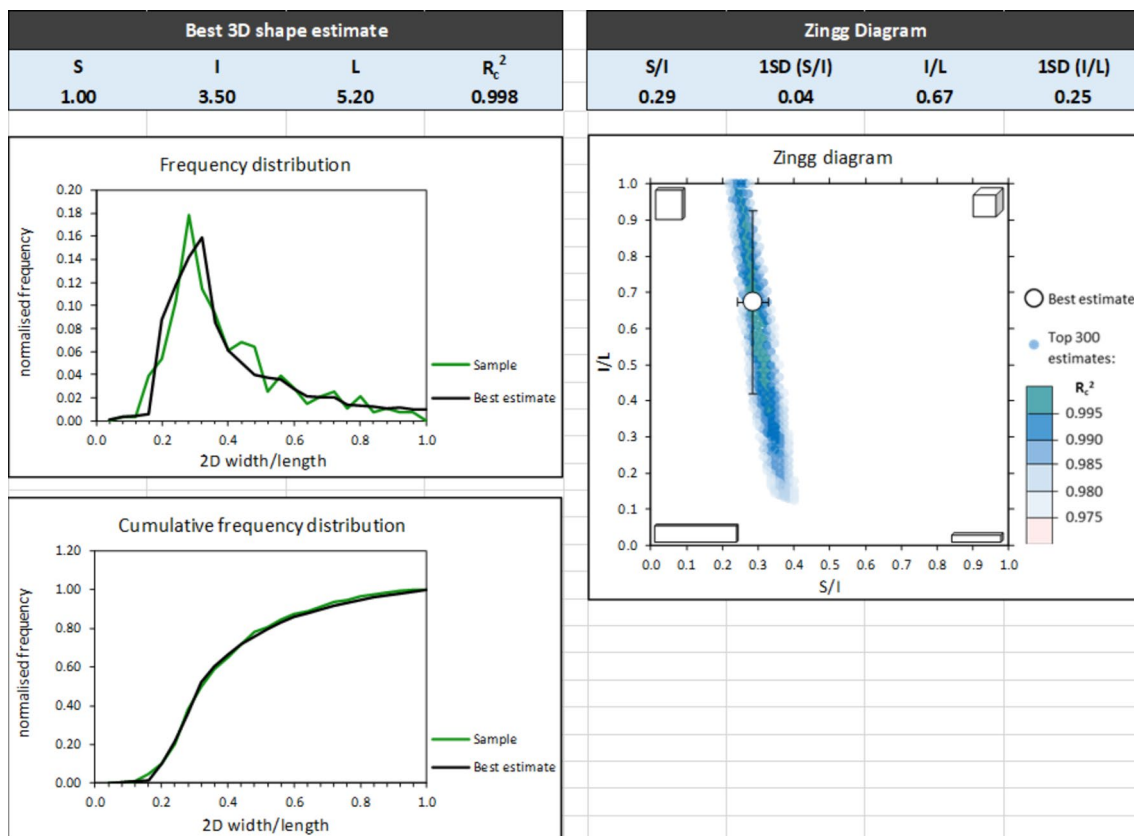


Fig. 3 Screen shot of *ShapeCalc* showing a good sample-model fit ($R_c^2 = 0.998$)

Table 1 3D shape estimates for Mt. St. Helens, Santiaguigo and Galeras samples. Galeras data is reprocessed from Bain et al. (2019; 2021)

Sample	System	Type	Eruption date	Fraction	<i>n</i>	%	<i>S</i>	<i>I</i>	<i>L</i>	R_c^2	<i>S/I</i>	± 1 SD*	<i>I/L</i>	± 1 SD*
SH52-2	Mt. St. Helens	1980–86 dome	Dec 1980	0–5 μm	770	39	1	1.25	4.40	0.993	0.80	± 0.08	0.28	± 0.14
SH52-2	Mt. St. Helens	1980–86 dome	Dec 1980	5–10 μm	512	26	1	2.20	6.40	0.977	0.45	± 0.07	0.34	± 0.25
SH52-2	Mt. St. Helens	1980–86 dome	Dec 1980	10–30 μm	414	21	1	2.70	5.60	0.978	0.37	± 0.06	0.48	± 0.25
SH52-2	Mt. St. Helens	1980–86 dome	Dec 1980	30–100 μm	278	14	1	3.50	9.60	0.998	0.29	± 0.04	0.36	± 0.24
SH52-2	Mt. St. Helens	1980–86 dome	Dec 1980	All	1974	100	n.a	n.a	n.a	0.963	n.a	± n.a	n.a	± n.a
MSH 90–9	Mt. St. Helens	1980–86 dome	1982	0–5 μm	314	22	1	1.15	2.80	0.994	0.87	± 0.10	0.41	± 0.22
MSH 90–9	Mt. St. Helens	1980–86 dome	1982	5–10 μm	336	24	1	1.75	6.00	0.976	0.57	± 0.06	0.29	± 0.18
MSH 90–9	Mt. St. Helens	1980–86 dome	1982	10–30 μm	430	30	1	2.40	5.00	0.980	0.42	± 0.07	0.48	± 0.26
MSH 90–9	Mt. St. Helens	1980–86 dome	1982	30–100 μm	346	24	1	3.50	6.80	0.998	0.29	± 0.04	0.51	± 0.25
MSH 90–9	Mt. St. Helens	1980–86 dome	1982	All	1426	100	n.a	n.a	n.a	0.969	n.a	± n.a	n.a	± n.a
SH131A-2	Mt. St. Helens	1980–86 dome	Aug 1982	0–5 μm	698	28	1	1.05	2.20	0.998	0.95	± 0.10	0.48	± 0.28
SH131A-2	Mt. St. Helens	1980–86 dome	Aug 1982	5–10 μm	752	30	1	1.45	4.40	0.991	0.69	± 0.07	0.33	± 0.22
SH131A-2	Mt. St. Helens	1980–86 dome	Aug 1982	10–30 μm	673	27	1	2.20	4.80	0.983	0.45	± 0.07	0.46	± 0.25
SH131A-2	Mt. St. Helens	1980–86 dome	Aug 1982	30–100 μm	354	14	1	3.60	6.40	0.997	0.28	± 0.04	0.56	± 0.25
SH131A-2	Mt. St. Helens	1980–86 dome	Aug 1982	All	2477	100	1	1.60	5.00	0.976	0.63	± 0.06	0.32	± 0.17
SH157	Mt. St. Helens	1980–86 dome	June 1984	0–5 μm	994	40	1	1.20	3.40	0.998	0.83	± 0.08	0.35	± 0.15
SH157	Mt. St. Helens	1980–86 dome	June 1984	5–10 μm	714	28	1	1.40	3.60	0.991	0.71	± 0.07	0.39	± 0.20
SH157	Mt. St. Helens	1980–86 dome	June 1984	10–30 μm	526	21	1	1.95	4.40	0.982	0.51	± 0.07	0.44	± 0.24
SH157	Mt. St. Helens	1980–86 dome	June 1984	30–100 μm	280	11	1	3.50	5.20	0.998	0.29	± 0.04	0.67	± 0.25
SH157	Mt. St. Helens	1980–86 dome	June 1984	All	2514	100	1	1.50	5.00	0.983	0.67	± 0.07	0.30	± 0.18
SH226	Mt. St. Helens	1980–86 dome	Oct 1986	0–5 μm	20	3	n.a	n.a	n.a	n.a	n.a	± n.a	n.a	± n.a
SH226	Mt. St. Helens	1980–86 dome	Oct 1986	5–10 μm	50	9	n.a	n.a	n.a	n.a	n.a	± n.a	n.a	± n.a
SH226	Mt. St. Helens	1980–86 dome	Oct 1986	10–30 μm	200	35	1	1.45	3.80	0.988	0.69	± 0.08	0.38	± 0.23
SH226	Mt. St. Helens	1980–86 dome	Oct 1986	30–100 μm	305	53	1	2.50	4.40	0.995	0.40	± 0.06	0.57	± 0.26
SH226	Mt. St. Helens	1980–86 dome	Oct 1986	> 100 μm	96		1	2.40	4.60	0.996	0.42	± 0.06	0.52	± 0.26
SH226	Mt. St. Helens	1980–86 dome	Oct 1986	All	671		1	2.10	3.80	0.982	0.48	± 0.07	0.55	± 0.25
SG-09-04	Santiaguigo	Lava flow	2000	0–5 μm	821	38	1	1.20	3.80	0.997	0.83	± 0.08	0.32	± 0.15
SG-09-04	Santiaguigo	Lava flow	2000	5–10 μm	631	29	1	2.80	5.60	0.981	0.36	± 0.06	0.50	± 0.25
SG-09-04	Santiaguigo	Lava flow	2000	10–30 μm	588	27	1	7.00	9.60	0.993	0.14	± 0.03	0.73	± 0.23
SG-09-04	Santiaguigo	Lava flow	2000	30–100 μm	145	7	n.a	n.a	n.a	0.946	n.a	± n.a	n.a	± n.a
SG-09-04	Santiaguigo	Lava flow	2000	All	2185	100	n.a	n.a	n.a	0.889	n.a	± n.a	n.a	± n.a
SG-09-06	Santiaguigo	Lava flow	1986–1989	0–5 μm	734	41	1	1.25	4.40	0.996	0.80	± 0.08	0.28	± 0.14
SG-09-06	Santiaguigo	Lava flow	1986–1989	5–10 μm	472	26	1	2.70	5.60	0.976	0.37	± 0.06	0.48	± 0.25
SG-09-06	Santiaguigo	Lava flow	1986–1989	10–30 μm	474	27	1	6.20	8.80	0.992	0.16	± 0.03	0.70	± 0.23
SG-09-06	Santiaguigo	Lava flow	1986–1989	30–100 μm	104	6	1	9.40	20.0	0.991	0.11	± 0.03	0.47	± 0.19
SG-09-06	Santiaguigo	Lava flow	1986–1989	All	1784	100	n.a	n.a	n.a	0.898	n.a	± n.a	n.a	± n.a
GAL4	Galeras	Scoriaceous bomb	2004–2010	0–5 μm	372	25	1	1.30	3.20	0.999	0.77	± 0.07	0.41	± 0.22

Table 1 (continued)

Sample	System	Type	Eruption date	Fraction	n	%	S	I	L	R _c ²	S/I	±	1 SD*	I/L	±	1 SD*
GAL4	Galeras	Scoriaceous bomb	2004–2010	5–10 µm	463	31	1	1.95	4.40	0.994	0.51	±	0.06	0.44	±	0.24
GAL4	Galeras	Scoriaceous bomb	2004–2010	10–30 µm	546	37	1	3.10	7.20	0.982	0.32	±	0.05	0.43	±	0.25
GAL4	Galeras	Scoriaceous bomb	2004–2010	30–100 µm	109	7	1	4.80	9.20	0.987	0.21	±	0.03	0.52	±	0.21
GAL4	Galeras	Scoriaceous bomb	2004–2010	All	1490	100	n.a	n.a	n.a	0.974	n.a	±	n.a	n.a	±	n.a
GAL5	Galeras	Dense bomb	2004–2010	0–5 µm	2188	66	1	1.30	2.80	0.999	0.77	±	0.08	0.46	±	0.26
GAL5	Galeras	Dense bomb	2004–2010	5–10 µm	759	23	1	1.65	5.60	0.995	0.61	±	0.06	0.29	±	0.20
GAL5	Galeras	Dense bomb	2004–2010	10–30 µm	299	9	1	1.95	5.60	0.990	0.51	±	0.06	0.35	±	0.24
GAL5	Galeras	Dense bomb	2004–2010	30–100 µm	65	2	1	2.10	4.20	0.991	0.48	±	0.06	0.50	±	0.25
GAL5	Galeras	Dense bomb	2004–2010	All	3311	100	1	1.40	4.20	0.998	0.71	±	0.07	0.33	±	0.21
GAL6	Galeras	Scoriaceous bomb	2004–2010	0–5 µm	444	41	1	1.40	3.60	0.997	0.71	±	0.07	0.39	±	0.22
GAL6	Galeras	Scoriaceous bomb	2004–2010	5–10 µm	339	31	1	1.85	5.00	0.993	0.54	±	0.06	0.37	±	0.22
GAL6	Galeras	Scoriaceous bomb	2004–2010	10–30 µm	267	25	1	2.80	5.60	0.975	0.36	±	0.06	0.50	±	0.25
GAL6	Galeras	Scoriaceous bomb	2004–2010	30–100 µm	38	3	n.a	n.a	n.a	n.a	n.a	±	n.a	n.a	±	n.a
GAL6	Galeras	Scoriaceous bomb	2004–2010	All	1088	100	1	1.75	6.00	0.987	0.57	±	0.06	0.29	±	0.18
GAL7	Galeras	Scoriaceous bomb	2004–2010	0–5 µm	306	40	1	1.55	5.00	0.998	0.65	±	0.06	0.31	±	0.21
GAL7	Galeras	Scoriaceous bomb	2004–2010	5–10 µm	205	27	1	1.70	4.20	0.996	0.59	±	0.06	0.40	±	0.22
GAL7	Galeras	Scoriaceous bomb	2004–2010	10–30 µm	208	27	1	3.00	6.40	0.980	0.33	±	0.05	0.47	±	0.25
GAL7	Galeras	Scoriaceous bomb	2004–2010	30–100 µm	42	6	n.a	n.a	n.a	n.a	n.a	±	n.a	n.a	±	n.a
GAL7	Galeras	Scoriaceous bomb	2004–2010	All	761	100	1	1.80	6.40	0.986	0.56	±	0.06	0.28	±	0.20
GAL8	Galeras	Scoriaceous bomb	2004–2010	0–5 µm	958	54	1	1.35	3.40	0.997	0.74	±	0.07	0.40	±	0.23
GAL8	Galeras	Scoriaceous bomb	2004–2010	5–10 µm	448	25	1	1.65	8.80	0.988	0.61	±	0.06	0.19	±	0.18
GAL8	Galeras	Scoriaceous bomb	2004–2010	10–30 µm	324	18	n.a	n.a	n.a	0.973	n.a	±	n.a	n.a	±	n.a
GAL8	Galeras	Scoriaceous bomb	2004–2010	30–100 µm	50	3	n.a	n.a	n.a	n.a	n.a	±	n.a	n.a	±	n.a
GAL8	Galeras	Scoriaceous bomb	2004–2010	All	1780	100	1	1.60	5.20	0.986	0.63	±	0.06	0.31	±	0.17
GAL14	Galeras	Scoriaceous bomb	2004–2010	0–5 µm	443	53	1	1.40	3.20	0.998	0.71	±	0.08	0.44	±	0.25
GAL14	Galeras	Scoriaceous bomb	2004–2010	5–10 µm	211	25	1	1.75	6.00	0.994	0.57	±	0.06	0.29	±	0.20
GAL14	Galeras	Scoriaceous bomb	2004–2010	10–30 µm	146	18	n.a	n.a	n.a	0.957	n.a	±	n.a	n.a	±	n.a
GAL14	Galeras	Scoriaceous bomb	2004–2010	30–100 µm	29	3	n.a	n.a	n.a	n.a	n.a	±	n.a	n.a	±	n.a
GAL14	Galeras	Scoriaceous bomb	2004–2010	All	829	100	1	1.60	5.20	0.992	0.63	±	0.06	0.31	±	0.19
GAL16	Galeras	Scoriaceous bomb	2004–2010	0–5 µm	539	47	1	1.40	2.40	0.999	0.71	±	0.08	0.58	±	0.27
GAL16	Galeras	Scoriaceous bomb	2004–2010	5–10 µm	309	27	1	1.85	5.20	0.994	0.54	±	0.06	0.36	±	0.22
GAL16	Galeras	Scoriaceous bomb	2004–2010	10–30 µm	255	22	n.a	n.a	n.a	0.973	n.a	±	n.a	n.a	±	n.a
GAL16	Galeras	Scoriaceous bomb	2004–2010	30–100 µm	38	3	n.a	n.a	n.a	n.a	n.a	±	n.a	n.a	±	n.a
GAL16	Galeras	Scoriaceous bomb	2004–2010	All	1141	100	1	1.60	5.20	0.992	0.63	±	0.06	0.31	±	0.18
GAL18	Galeras	Scoriaceous bomb	2004–2010	0–5 µm	833	54	1	1.45	4.40	0.998	0.69	±	0.07	0.33	±	0.21
GAL18	Galeras	Scoriaceous bomb	2004–2010	5–10 µm	387	25	1	2.10	6.00	0.991	0.48	±	0.06	0.35	±	0.24

Table 1 (continued)

Sample	System	Type	Eruption date	Fraction	<i>n</i>	%	<i>S</i>	<i>I</i>	<i>L</i>	R_c^2	<i>S/I</i>	±	1 SD*	<i>I/L</i>	±	1 SD*
GAL18	Galeras	Scoriaceous bomb	2004–2010	10–30 µm	275	18	n.a	n.a	n.a	0.977	n.a	±	n.a	n.a	±	n.a
GAL18	Galeras	Scoriaceous bomb	2004–2010	30–100 µm	51	3	n.a	n.a	n.a	n.a	n.a	±	n.a	n.a	±	n.a
GAL18	Galeras	Scoriaceous bomb	2004–2010	All	1546	100	1	1.80	6.40	0.981	0.56	±	0.06	0.28	±	0.17
AB2	Galeras	Dense bomb	11–12-Aug-04	0–5 µm	432	36	1	1.30	2.40	0.999	0.77	±	0.09	0.54	±	0.27
AB2	Galeras	Dense bomb	11–12-Aug-04	5–10 µm	362	30	1	1.65	4.40	0.994	0.61	±	0.06	0.38	±	0.23
AB2	Galeras	Dense bomb	11–12-Aug-04	10–30 µm	326	27	1	2.80	5.60	0.991	0.36	±	0.06	0.50	±	0.25
AB2	Galeras	Dense bomb	11–12-Aug-04	30–100 µm	73	6	1	3.10	6.00	0.987	0.32	±	0.05	0.52	±	0.25
AB2	Galeras	Dense bomb	11–12-Aug-04	All	1193	100	1	1.65	5.60	0.988	0.61	±	0.06	0.29	±	0.18
AB4bis	Galeras	Inflated bomb rind	11–12-Aug-04	0–5 µm	863	54	1	1.35	4.40	0.999	0.74	±	0.07	0.31	±	0.20
AB4bis	Galeras	Inflated bomb rind	11–12-Aug-04	5–10 µm	391	27	1	1.65	6.40	0.996	0.61	±	0.06	0.26	±	0.20
AB4bis	Galeras	Inflated bomb rind	11–12-Aug-04	10–30 µm	305	21	1	2.80	6.40	0.992	0.36	±	0.05	0.44	±	0.25
AB4bis	Galeras	Inflated bomb rind	11–12-Aug-04	30–100 µm	50	4	n.a	n.a	n.a	n.a	n.a	±	n.a	n.a	±	n.a
AB4bis	Galeras	Inflated bomb rind	11–12-Aug-04	All	1609	100	1	1.60	5.20	0.990	0.63	±	0.06	0.31	±	0.18
AB5b	Galeras	Scoriaceous bomb	21-Nov-04	0–5 µm	448	45	1	1.40	2.90	0.999	0.71	±	0.07	0.48	±	0.26
AB5b	Galeras	Scoriaceous bomb	21-Nov-04	5–10 µm	292	29	1	1.80	5.00	0.994	0.56	±	0.06	0.36	±	0.22
AB5b	Galeras	Scoriaceous bomb	21-Nov-04	10–30 µm	212	21	1	3.30	7.60	0.988	0.30	±	0.04	0.43	±	0.25
AB5b	Galeras	Scoriaceous bomb	21-Nov-04	30–100 µm	40	4	n.a	n.a	n.a	n.a	n.a	±	n.a	n.a	±	n.a
AB5b	Galeras	Scoriaceous bomb	21-Nov-04	All	992	100	1	1.65	8.80	0.987	0.61	±	0.06	0.19	±	0.17
AB6	Galeras	Inflated bomb rind	21-Nov-04	0–5 µm	969	53	1	1.35	2.50	0.999	0.74	±	0.08	0.54	±	0.26
AB6	Galeras	Inflated bomb rind	21-Nov-04	5–10 µm	437	24	1	1.80	4.80	0.992	0.56	±	0.06	0.38	±	0.22
AB6	Galeras	Inflated bomb rind	21-Nov-04	10–30 µm	345	19	n.a	n.a	n.a	0.973	n.a	±	n.a	n.a	±	n.a
AB6	Galeras	Inflated bomb rind	21-Nov-04	30–100 µm	76	4	1	3.10	8.80	0.986	0.32	±	0.05	0.35	±	0.25
AB6	Galeras	Inflated bomb rind	21-Nov-04	All	1827	100	1	1.45	12.0	0.990	0.69	±	0.06	0.12	±	0.17
AB8bis	Galeras	Scoriaceous bomb	12-Jul-06	0–5 µm	413	38	1	1.30	2.00	0.999	0.77	±	0.10	0.65	±	0.25
AB8bis	Galeras	Scoriaceous bomb	12-Jul-06	5–10 µm	332	31	1	1.75	4.00	0.999	0.57	±	0.06	0.44	±	0.23
AB8bis	Galeras	Scoriaceous bomb	12-Jul-06	10–30 µm	269	25	n.a	n.a	n.a	0.962	n.a	±	n.a	n.a	±	n.a
AB8bis	Galeras	Scoriaceous bomb	12-Jul-06	30–100 µm	60	6	n.a	n.a	n.a	0.975	n.a	±	n.a	n.a	±	n.a
AB8bis	Galeras	Scoriaceous bomb	12-Jul-06	All	1074	100	1	1.50	7.20	0.994	0.67	±	0.06	0.21	±	0.18
AB9bis	Galeras	Scoriaceous bomb	12-Jul-06	0–5 µm	448	44	1	1.30	3.60	0.999	0.77	±	0.07	0.36	±	0.21
AB9bis	Galeras	Scoriaceous bomb	12-Jul-06	5–10 µm	304	30	1	1.95	5.60	0.995	0.51	±	0.06	0.35	±	0.24
AB9bis	Galeras	Scoriaceous bomb	12-Jul-06	10–30 µm	227	22	n.a	n.a	n.a	0.971	n.a	±	n.a	n.a	±	n.a
AB9bis	Galeras	Scoriaceous bomb	12-Jul-06	30–100 µm	45	4	n.a	n.a	n.a	n.a	n.a	±	n.a	n.a	±	n.a
AB9bis	Galeras	Scoriaceous bomb	12-Jul-06	All	1024	100	1	1.65	6.40	0.984	0.61	±	0.06	0.26	±	0.18
AB10bis	Galeras	Inflated bomb rind	17-Jan-08	0–5 µm	2485	70	1	1.35	2.80	0.999	0.74	±	0.08	0.48	±	0.25
AB10bis	Galeras	Inflated bomb rind	17-Jan-08	5–10 µm	679	19	1	1.60	5.20	0.996	0.63	±	0.06	0.31	±	0.21
AB10bis	Galeras	Inflated bomb rind	17-Jan-08	10–30 µm	336	9	1	1.95	5.60	0.988	0.51	±	0.06	0.35	±	0.19

Table 1 (continued)

Sample	System	Type	Eruption date	Fraction	<i>n</i>	%	<i>S</i>	<i>I</i>	<i>L</i>	R_c^2	<i>S/I</i>	± 1 SD*	<i>I/L</i>	±	1 SD*
AB10bis	Galeras	Inflated bomb rind	17-Jan-08	30–100 µm	59	2	n.a	n.a	n.a	0.974	n.a	±	n.a	±	n.a
AB10bis	Galeras	Inflated bomb rind	17-Jan-08	All	3559	100	1	1.40	4.20	0.998	0.71	±	0.33	±	0.21
AB14bis	Galeras	Scoriaceous bomb	17-Jan-08	0–5 µm	485	33	1	1.50	2.00	0.998	0.67	±	0.75	±	0.27
AB14bis	Galeras	Scoriaceous bomb	17-Jan-08	5–10 µm	493	33	1	1.60	3.60	0.997	0.63	±	0.44	±	0.24
AB14bis	Galeras	Scoriaceous bomb	17-Jan-08	10–30 µm	442	30	1	2.40	5.00	0.986	0.42	±	0.48	±	0.25
AB14bis	Galeras	Scoriaceous bomb	17-Jan-08	30–100 µm	61	4	n.a	n.a	n.a	0.974	n.a	±	n.a	±	n.a
AB14bis	Galeras	Scoriaceous bomb	17-Jan-08	All	1481	100	1	1.60	5.00	0.994	0.63	±	0.32	±	0.19
AB15	Galeras	Scoriaceous bomb	17-Jan-08	0–5 µm	384	45	1	1.35	2.40	0.997	0.74	±	0.56	±	0.27
AB15	Galeras	Scoriaceous bomb	17-Jan-08	5–10 µm	243	29	1	1.60	3.60	0.997	0.63	±	0.44	±	0.23
AB15	Galeras	Scoriaceous bomb	17-Jan-08	10–30 µm	188	22	1	2.70	7.20	0.991	0.37	±	0.38	±	0.25
AB15	Galeras	Scoriaceous bomb	17-Jan-08	30–100 µm	31	4	n.a	n.a	n.a	n.a	n.a	±	n.a	±	n.a
AB15	Galeras	Scoriaceous bomb	17-Jan-08	All	846	100	1	1.45	12.0	0.992	0.69	±	0.12	±	0.18
AB16	Galeras	Inflated bomb rind	20-Feb-09	0–5 µm	936	55	1	1.35	2.50	0.999	0.74	±	0.54	±	0.27
AB16	Galeras	Inflated bomb rind	20-Feb-09	5–10 µm	470	27	1	1.60	5.00	0.996	0.63	±	0.32	±	0.20
AB16	Galeras	Inflated bomb rind	20-Feb-09	10–30 µm	274	16	n.a	n.a	n.a	0.973	n.a	±	n.a	±	n.a
AB16	Galeras	Inflated bomb rind	20-Feb-09	30–100 µm	37	2	n.a	n.a	n.a	n.a	n.a	±	n.a	±	n.a
AB16	Galeras	Inflated bomb rind	20-Feb-09	All	1717	100	1	1.45	4.80	0.998	0.69	±	0.30	±	0.20
AB18bis	Galeras	Dense bomb	20-Feb-09	0–5 µm	1045	57	1	1.30	2.30	0.999	0.77	±	0.57	±	0.27
AB18bis	Galeras	Dense bomb	20-Feb-09	5–10 µm	466	25	1	1.60	5.20	0.996	0.63	±	0.31	±	0.20
AB18bis	Galeras	Dense bomb	20-Feb-09	10–30 µm	288	16	1	2.00	9.60	0.990	0.50	±	0.21	±	0.24
AB18bis	Galeras	Dense bomb	20-Feb-09	30–100 µm	39	2	n.a	n.a	n.a	n.a	n.a	±	n.a	±	n.a
AB18bis	Galeras	Dense bomb	20-Feb-09	All	1838	100	1	1.45	3.80	0.999	0.69	±	0.38	±	0.22
AB21	Galeras	Dense bomb	02-Jan-10	0–5 µm	1571	55	1	1.30	2.60	0.999	0.77	±	0.50	±	0.26
AB21	Galeras	Dense bomb	02-Jan-10	5–10 µm	740	26	1	1.65	5.60	0.995	0.61	±	0.29	±	0.20
AB21	Galeras	Dense bomb	02-Jan-10	10–30 µm	473	16	n.a	n.a	n.a	0.974	n.a	±	n.a	±	n.a
AB21	Galeras	Dense bomb	02-Jan-10	30–100 µm	88	3	1	3.60	7.20	0.981	0.28	±	0.50	±	0.25
AB21	Galeras	Dense bomb	02-Jan-10	All	2872	100	1	1.45	6.80	0.996	0.69	±	0.21	±	0.18
AB22	Galeras	Inflated bomb rind	02-Jan-10	0–5 µm	1685	48	1	1.95	5.60	0.979	0.51	±	0.35	±	0.22
AB22	Galeras	Inflated bomb rind	02-Jan-10	5–10 µm	1229	35	1	4.60	8.80	0.992	0.22	±	0.52	±	0.21
AB22	Galeras	Inflated bomb rind	02-Jan-10	10–30 µm	571	16	1	6.60	19.0	0.988	0.15	±	0.35	±	0.21
AB22	Galeras	Inflated bomb rind	02-Jan-10	30–100 µm	8	0	n.a	n.a	n.a	n.a	n.a	±	n.a	±	n.a
AB22	Galeras	Inflated bomb rind	02-Jan-10	All	3493	100	n.a	n.a	n.a	0.964	n.a	±	n.a	±	n.a

n.a. Insufficient number of crystals (*n* < 50) or $R_c^2 > 0.975$

* 1 SD on average of estimates with $R_c^2 > 0.975$

smallest crystals ($l=0\text{--}5\ \mu\text{m}$) approach prismatic shapes ($S/I=0.7\text{--}1$), whereas the largest fractions analysed ($l=30\text{--}100\ \mu\text{m}$) are tabular with $S/I=0.1\text{--}0.4$. Typical uncertainties are $\pm 0.03\text{--}0.10$ for S/I and $\pm 0.14\text{--}0.28$ for I/L . All samples show the same trend, however absolute S/I values for different fractions vary, both between volcanic systems and between different samples from the same system. In addition, data for Mt. St. Helens and Santiaguigo trace an increase in I/L for larger size fractions, suggesting increased I at relatively stable S/L (Fig. 4a–c). No clear correlation between S/I and I/L for different size fractions is observed at Galeras (Fig. 4d), which may be due in part two to three times larger uncertainties for I/L than for S/I . The change from high- S/I (prismatic shapes) to low- S/I

(tabular shapes) with increasing crystal size is therefore robustly documented by the data, whereas changes in the longest dimension of the respective shape (e.g., tabular vs. bladed) are less well constrained. Visual assessment of rock textures qualitatively confirms a trend towards lower S/I with increasing crystal size (Fig. 5). The $0\text{--}5\ \mu\text{m}$ fraction in Fig. 5b shows a markedly higher abundance of 2D intersections with $w\approx l$, whereas the $30\text{--}100\ \mu\text{m}$ fraction exhibits more elongate intersections with $w/l\approx 0.2\text{--}0.3$. We also tested whether the crystal shape variations observed for our samples could be generated by the w/l data binning process itself, but found no indication for such artefacts (Online Resource 5).

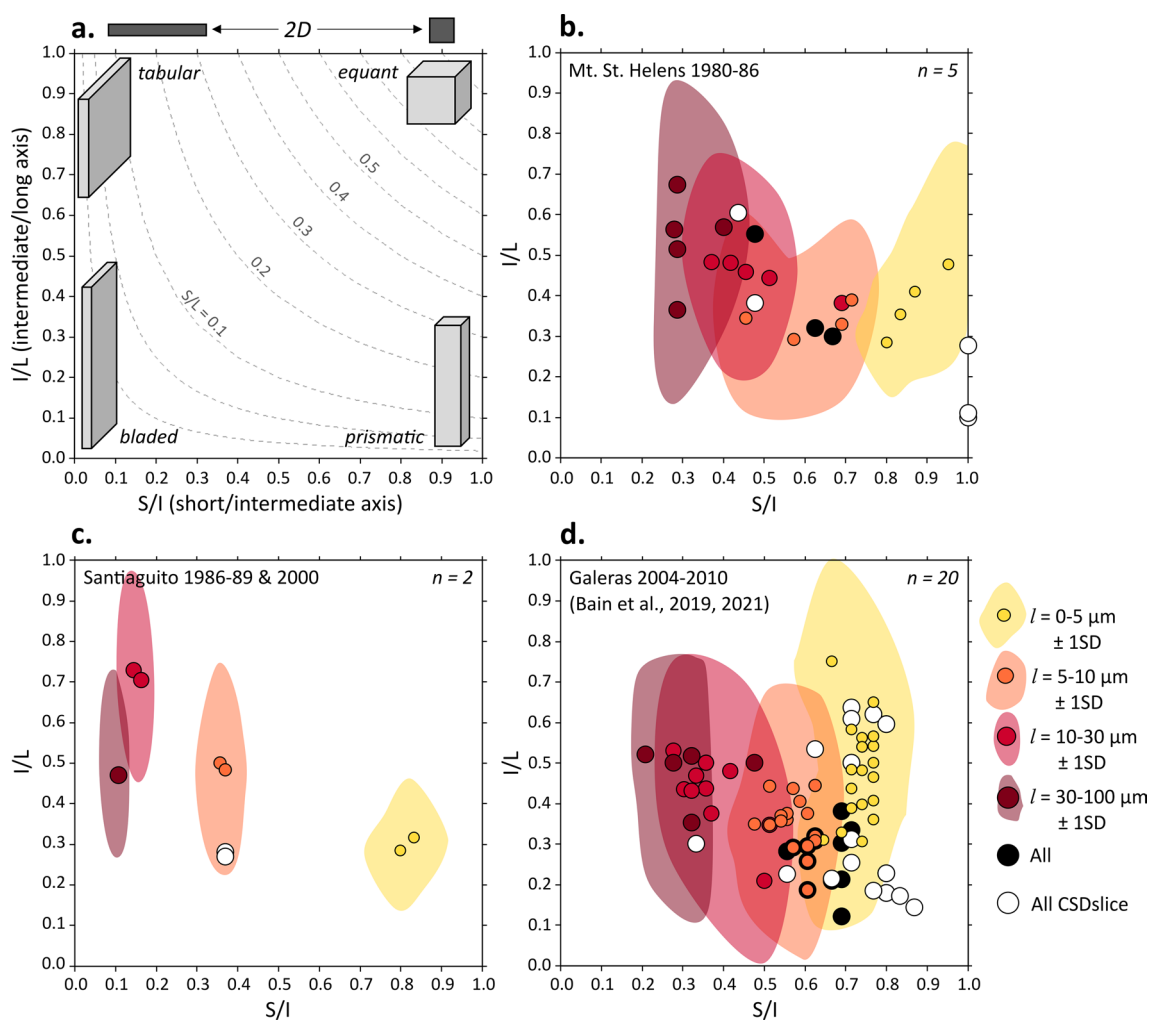


Fig. 4 (a) Blank Zingg diagram. In a Zingg diagram, the 3D intermediate to long axis ratio I/L is plotted against the 3D short to intermediate axis S/I to fully describe the shape of 3D objects. The dominant 2D expression of respective 3D shapes is indicated on top of the diagram. (b–d) Zingg diagrams showing 3D shape estimates for individual crystal size fractions obtained for n samples using *ShapeCalc*. (b) Mt. St. Helens, (c) Santiaguigo, (d) Galeras (Bain et al. 2019, 2021).

$l=0\text{--}5\ \mu\text{m}$ (yellow), $5\text{--}10\ \mu\text{m}$ (orange), $10\text{--}30\ \mu\text{m}$ (red), $30\text{--}100\ \mu\text{m}$ (dark red), and $0\text{--}100\ \mu\text{m}$ (black; unbinned dataset). Symbol sizes are schematically scaled to represent respective size fractions. Only 3D shape estimates with $R_c^2 > 0.975$ are shown. Unbinned shape estimates obtained by *CSDslice* (white) are also shown. A trend towards lower S/I with increasing crystal size is visible for all three case studies

In contrast, 3D shape estimates for the complete, unbinned datasets tend to produce poorer model fits, with several estimates showing $R_c^2 < 0.975$ (Table 1). Shape estimates with acceptable fits ($R_c^2 > 0.975$) overlap with those for the binned datasets, most commonly with the $l=5\text{--}10\ \mu\text{m}$ fraction (black circles in Fig. 4). On the other hand, conventional processing of the unbinned 2D dataset with *CSDslice* (white circles in Figs. 4, 5) yields shapes with $S \approx I$ that do not reflect any of the fractions in three out of five cases for Mt. St. Helens and in three cases for Galeras. Such shape results do not reflect any shapes of individual crystal fractions and are a combined artefact of a hybrid input population and the model w/l distributions used by *CSDslice* (Fig. 3d). Processing crystal size fraction data using *CSDslice* yields qualitatively similar patterns of decreasing S/I , albeit with significantly larger scatter and common defaulting to 1:1: L shapes (Online Resource 3).

Discussion

Correlation between crystal shape and number density

The increase in S/I towards smaller crystals coincides with a general increase in the number of crystal intersections in each fraction: for example, the 30–100 μm fraction of 1980–84 Mt. St. Helens rocks constitutes 11–24% of all crystal intersections, whereas the 0–5 μm fractions account for 22–40% (Fig. 6a–c; Table 1). The true number density for the smaller fractions is likely even higher, as larger crystals are more likely to be sectioned than smaller ones (intersection probability effect; Higgins 1994). Experimental constraints suggest that high number densities N_V are associated with high “effective” undercoolings ΔT_{eff} (i.e., the difference between mineral liquidus temperature and actual run temperature at (final) pressure; Hammer and

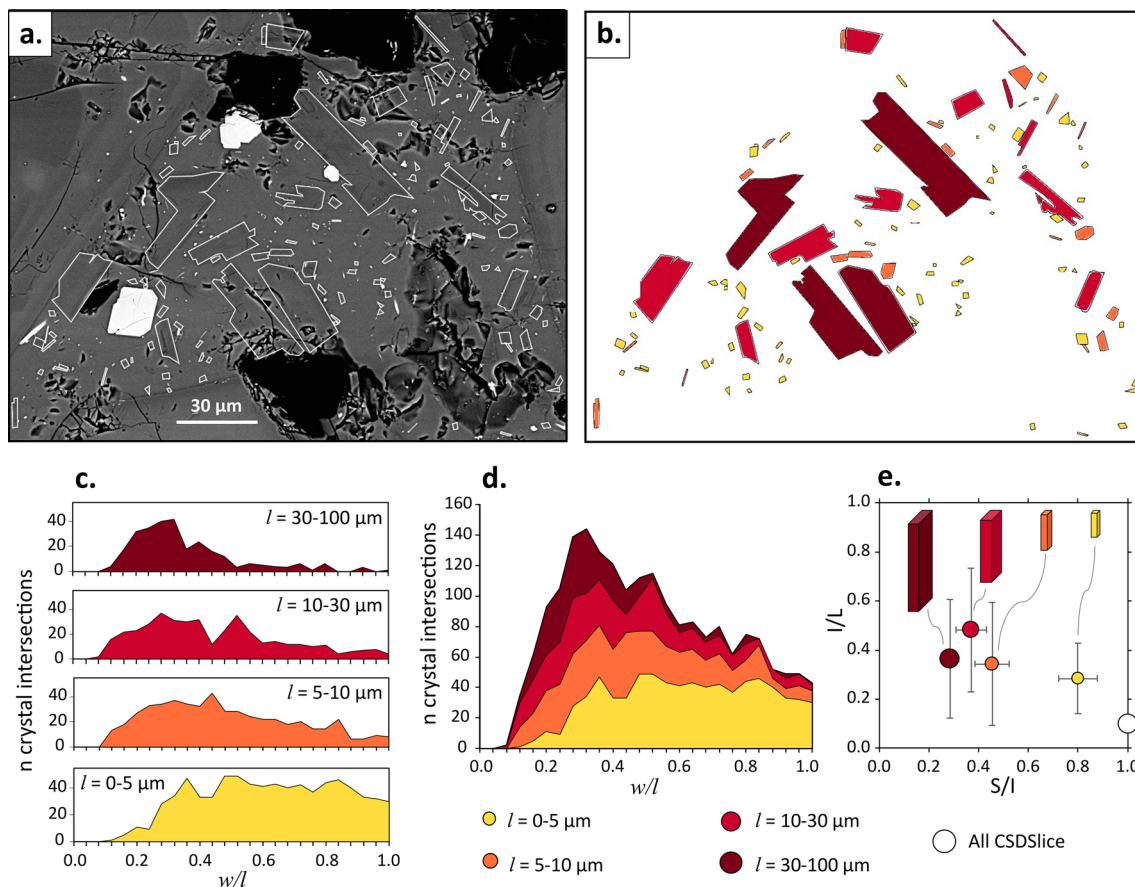


Fig. 5 Worked example for MSH sample SH52-2. (a) extract from a BSE image used for textural data acquisition. Plagioclase crystals are outlined in white for better visibility. (b) 2D crystal intersections colored by crystal size fractions. Note clear differences in w/l between fractions. (c) individual w/l distributions trace an increasingly dominant peak at $w/l \approx 0.2\text{--}0.3$ for larger size fractions. (d) Relative con-

tributions of each fraction to the unbinned w/l distribution. (e) Zingg diagram showing best 3D shape estimates obtained with *ShapeCalc*, as well as representative 3D models visualising respective shapes. Note that the unsorted *CSDslice* estimate (white circle) does not reflect any true crystal shape in the sample

Rutherford 2002), which in turn is commonly considered to produce low- S/I , tabular crystal habits (e.g., Lofgren 1974; Walker et al. 1976; Kirkpatrick et al. 1979; Shea and Hammer 2013). According to the established paradigm, we would therefore expect generally more *tabular* crystal habits as N_V increases, and specifically the *lowest* S/I for the fractions with the highest number densities 0–5 μm fractions. However, our shape results trace the opposite trend, with more *prismatic* habits as N_V increases, and the *highest* S/I for the 0–5 μm fractions (Figs. 4, 5).

It is crucial to note that the increasing N_V for smaller size fractions result in rapidly escalating *cumulative* number densities during crystallisation, since logic dictates that the largest crystal fractions crystallised first, and the smallest last (Fig. 6d–f). Indeed, rocks from many natural arc volcanoes exhibit high total N_V of up to 10^8 mm^{-3} (e.g., Pinatubo: Hammer et al. 1999; Soufriere Hills: Murch and Cole 2019; Mt. St. Helens: Cashman and McConnell 2005; Mt. Pelee: Martel and Poussineau 2007), which have been notoriously

difficult to reproduce in experiments (e.g., Cashman 2020; Lindoo and Cashman 2021). However, Martel (2012) experimentally reproduced both the high total N_V and the morphological variety of our natural samples by subjecting a rhyolitic melt to very low decompression rates of 0.003 MPa/min to low final pressures of $P_f = 5\text{--}10 \text{ MPa}$ ($\Delta T_{\text{eff}} > 275 \text{ }^\circ\text{C}$; D35 in Martel 2012). Strikingly, crystal shapes developed in these slowly decompressed, high- N_V experiments show a clear resemblance to our natural samples (Fig. 6f in Martel 2012), with an inferred range of $S/I \approx 0.3\text{--}1$. By contrast, slightly faster decompression (0.04 MPa/min) at otherwise identical run conditions produced lower N_V and generally lower S/I (i.e., more elongate 2D shapes; D37 in Martel 2012). These experimental results are consistent with our findings in natural samples. Importantly, the experimental suite produced by Martel (2012) shows no correlation between crystal morphologies and host glass compositions, ruling out variations in crystal growth regime as an explanation for the changes in crystal shape. Instead, we suggest that

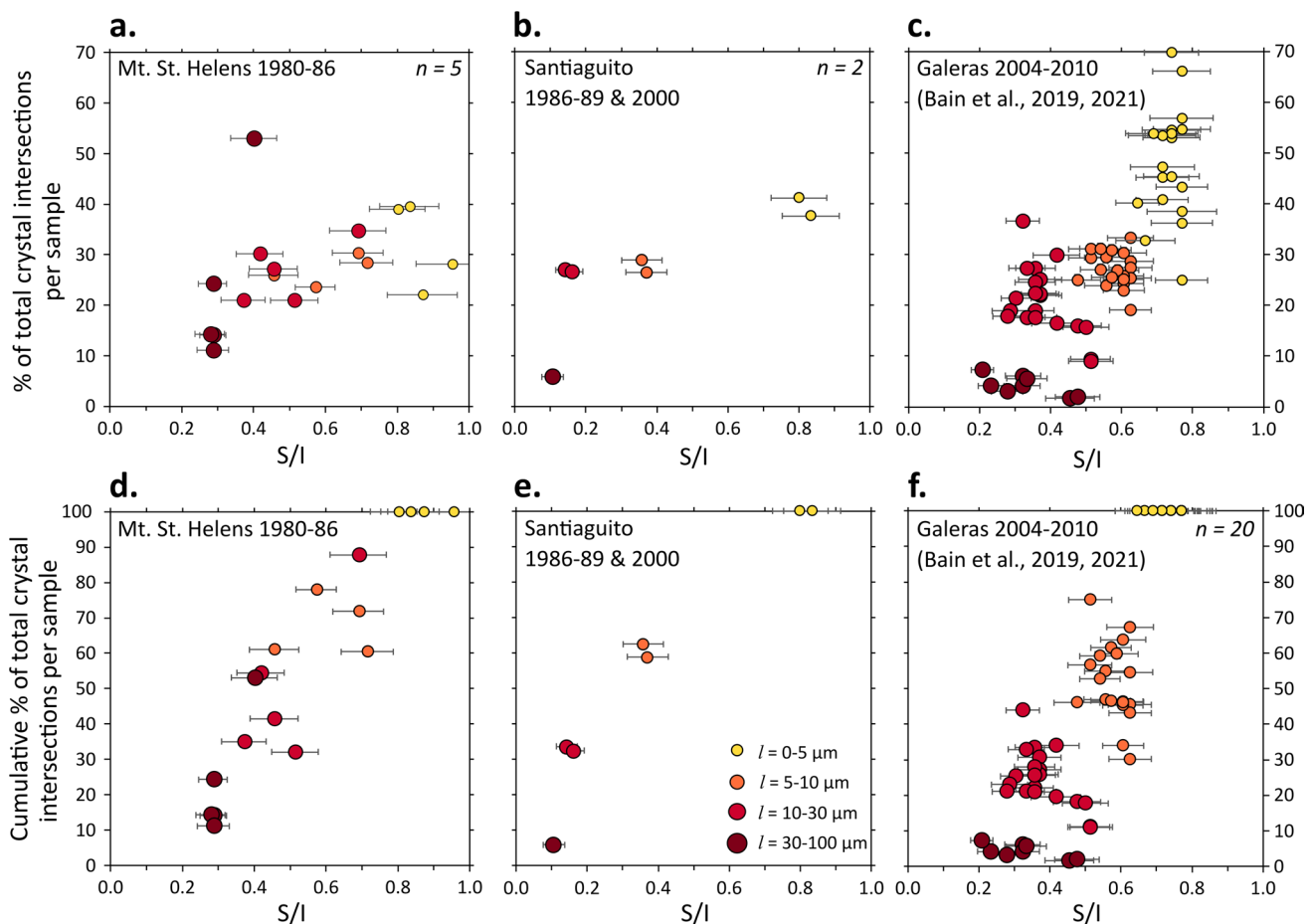


Fig. 6 (a–c) Proportions of crystal intersections by size fractions for n samples, plotted against S/I for (a) Mt. St. Helens, (b) Santiaguito, (c) Galeras (Bain et al. 2019, 2021). Note that number densities for individual fractions are generally higher for the smaller, high- S/I

fractions than for the larger, low- S/I fractions. (d–f) Cumulative % of crystal intersections, ordered by fractions of decreasing size, and plotted against S/I for (d) Mt. St. Helens, (e) Santiaguito, (f) Galeras (Bain et al. 2019, 2021)

the observed correlation between total crystal number density and crystal shapes points towards a causal relationship.

Crystal growth modelling

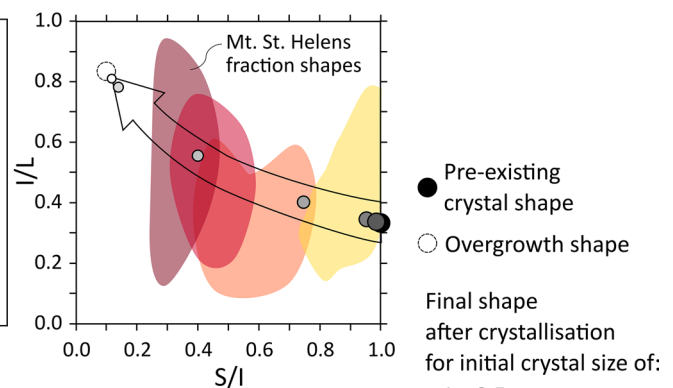
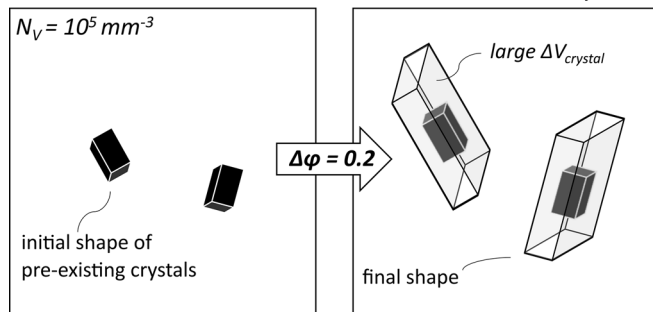
To explore this relationship further, we consider that for a given increase in crystallinity $\Delta\phi$ of a magma, induced by a given undercooling ΔT_{eff} , a higher N_V in the magma (i.e., the total number of both pre-existing and nucleating crystals) results in a reduction in the ‘growth volume’ available per crystal, $\Delta V_{crystal}$ (Andrews and Befus 2020; schematic in Fig. 7). Applied to our samples, the systematic change of crystal habit with cumulative N_V suggests that crystal shape may be controlled by $\Delta V_{crystal}$ and, by implication, that crystal shape systematically changes during growth. Is it possible, then, that the observed trend of decreasing S/I with increasing crystal size (Fig. 4) may simply trace the evolution of plagioclase morphology during growth? In other words, did the plagioclase tablets of the 30–100 μm fraction initially crystallise

as rods similar to those of the 0–5 μm fraction, and continue to evolve towards their final tabular shape?

To test this hypothesis, we modelled overgrowth of plagioclase rods with $S:I:L = 1:1:3$ by a typical tabular plagioclase shape ($S:I:L = 1:10:12$, Fig. 7). We tested the extent to which S/I of the external grain shape would evolve during 20% crystallisation of a magma for two endmember cases of naturally occurring number densities ($N_V = 10^5$ and 10^8 mm^{-3}) and a range of pre-existing crystal sizes ($I = 0.5\text{--}30 \mu\text{m}$). No new nucleation is considered in this simple model (see below).

For the case of low number density ($N_V = 10^5 \text{ mm}^{-3}$), the relatively large $\Delta V_{crystal}$ results in significant changes of crystal morphology during overgrowth for pre-existing crystals with $I \leq 10 \mu\text{m}$ (Fig. 7a). In particular, the smallest crystals ($I \leq 1 \mu\text{m}$) grow to thin tabular shapes with $S/I \sim 0.12$ and $I/L \sim 0.80$ (Fig. 7a), equivalent to the shapes of the 30–100 μm plagioclase fraction in natural samples. On the other hand, at high number densities typical for erupted rocks in volcanic arcs ($N_V = 10^8 \text{ mm}^{-3}$; Cashman et al. 2020), $\Delta V_{crystal}$ is lower and crystals $\leq 1 \mu\text{m}$ grow to shapes

a. Low & moderate number density: low $N_V/\Delta\phi$



b. Escalating number density: high $N_V/\Delta\phi$

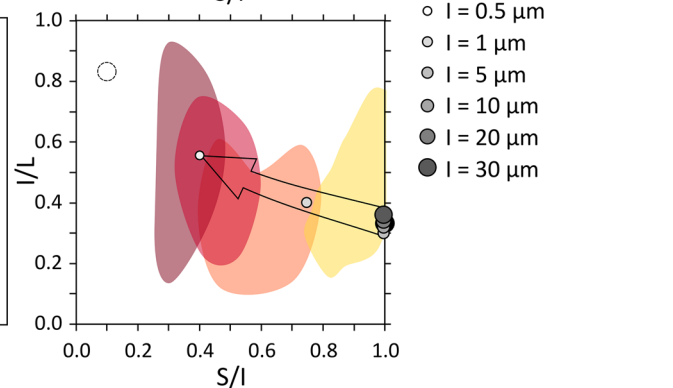
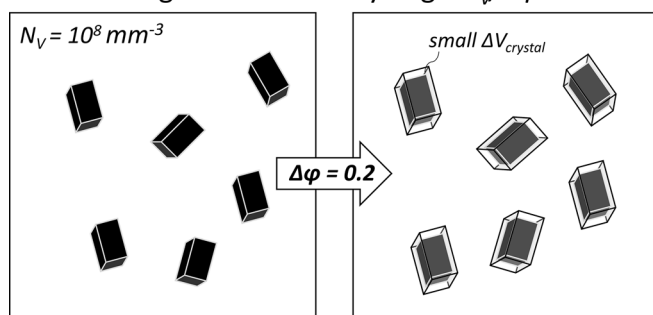


Fig. 7 Schematic and models of crystal shape evolution during 20 vol. % crystallisation and number densities of (a) $N_V = 10^5 \text{ mm}^{-3}$; (b) $N_V = 10^8 \text{ mm}^{-3}$. The model illustrates tabular overgrowth (1:10:12) of pre-existing prismatic crystals (1:1:3) with varying sizes ($I = 0.5\text{--}30 \mu\text{m}$). (a) Low number densities result in relatively large growth volumes per crystal, which therefore tend to develop tabular shapes.

If pre-existing prismatic crystals are small ($I \leq 1 \mu\text{m}$), growth results in tabular shapes approximating overgrowth proportions. (b) A high number of pre-existing crystals results in low growth volumes per crystal, and resulting shapes for small crystals ($I \leq 1 \mu\text{m}$) are closer to their prismatic starting shape. Larger crystals ($I > 10 \mu\text{m}$) do not change shape in either scenario

with lower S/I approximating those of the $\leq 10 \mu\text{m}$ fractions of natural plagioclase crystals (Fig. 7b). The models therefore show that the resulting final crystal shapes cover the entire range in S/I and I/L observed for our natural samples, depending on N_V and the sizes of pre-existing crystals. Adding some new nucleation alongside overgrowth of existing grains would dampen the calculated shape variations and

decrease the grainsize at which the shape of pre-existing crystals can be changed measurably.

These model results suggest that *nucleating* plagioclase crystals in the groundmass of intermediate magmas may have prismatic shapes, and that their final shape is controlled by the available growth volume per crystal $\Delta V_{crystal}$. Assuming that crystal growth rate is size-independent, $\Delta V_{crystal}$ can be expressed as the ratio between the number

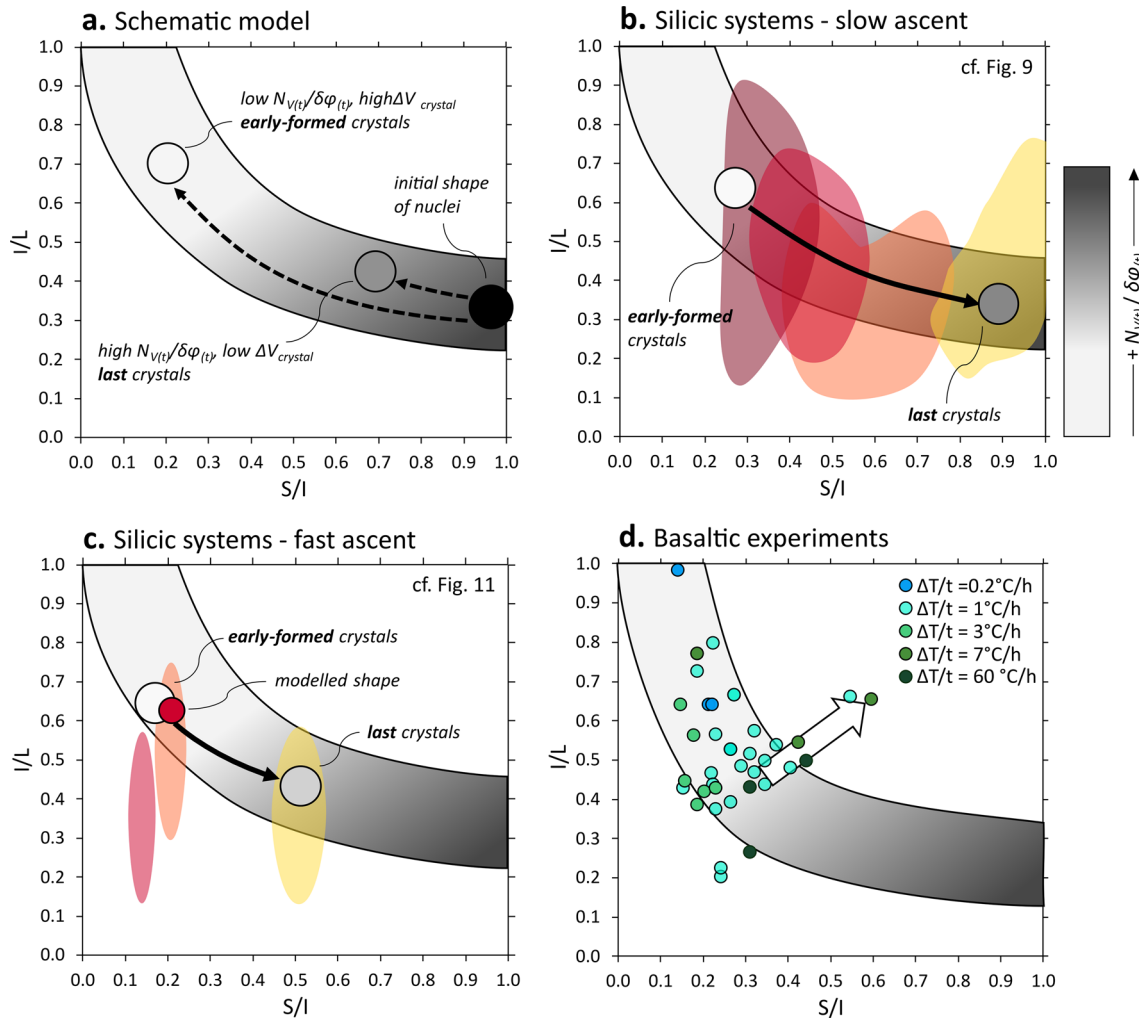


Fig. 8 (a) Schematic growth model relating plagioclase crystal shapes with available growth volumes $\Delta V_{crystal}$, which is a function of number density $N_{V(t)}$ and supersaturation $\delta\varphi_{(t)}$ at time t of nucleation. Low $N_{V(t)}/\delta\varphi_{(t)}$ impose high available growth volumes per crystal, and larger, tabular crystals develop. High $N_{V(t)}/\delta\varphi_{(t)}$ impose low available growth volumes per crystal, and smaller, prismatic crystals develop. Since $N_{V(t)}/\delta\varphi_{(t)}$ tends to increase in nucleating magmas, early-formed crystals develop more tabular shapes than those formed late during crystallisation. (b) Schematic model of the wide range of crystal shapes developed in an intermediate magma during slow ascent. Quasi-continuous nucleation during slow decompression results in a steady increase of $N_{V(t)}/\delta\varphi_{(t)}$ sampled by successive generations of nuclei. Coloured fields are microlite size fraction data for Mt. St. Helens (c.f. Figure 4). (c) Schematic model of the rela-

tively small range of crystal shapes typical for intermediate magmas that ascended rapidly before briefly stalling at shallow depth prior to eruption. Nucleation is suppressed during fast ascent, before a nucleation burst at shallow depth produces a large number of crystals with tabular shape, rapidly increasing crystallinity. Coloured fields are microlite size fraction data for Galeras sample AB22 (Bain et al. 2019); red circle is a model of plagioclase shapes formed for textural characteristics of AB22 ($\Delta\varphi=0.2$, $N_V=8 \times 10^6 \text{ mm}^{-3}$). (d) Experimental data for cooling of a basalt at cooling rates of 0.2–60 °C/h reprocessed from Pupier et al. (2008) and Giuliani et al. (2020) using *ShapeCalc*. Data from Pupier et al. (2008) is unbinned; data from Giuliani et al. (2020) is binned into fractions < 10 μm , 10–30 μm and 30–100 μm . Note the shift towards lower S/I in basaltic melts and the trend towards higher S/I at a given I/L (white arrow)

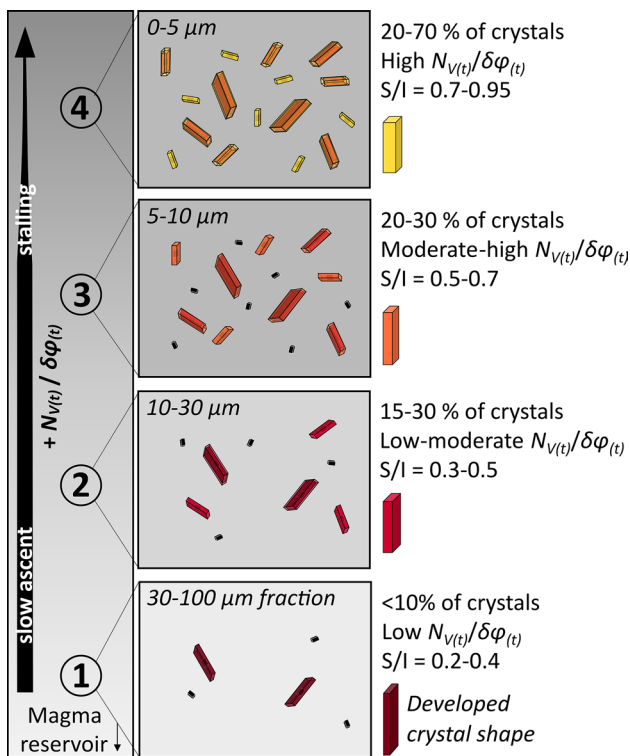


Fig. 9 Schematic model of the textural evolution of intermediate magmas during slow ascent. Early-stage nucleation deep in the conduit (Stage 1) and subsequent growth at low $N_{V(t)} / \Delta\phi(t)$ (i.e., large available growth volumes) produces crystals with tabular shapes. Increasing number densities during ascent-driven nucleation progressively decrease available growth volumes per crystal (Stages 2–3), such that crystals formed late-stage remain small and prismatic in shape (Stage 4). See Fig. 8b for and text for further explanation

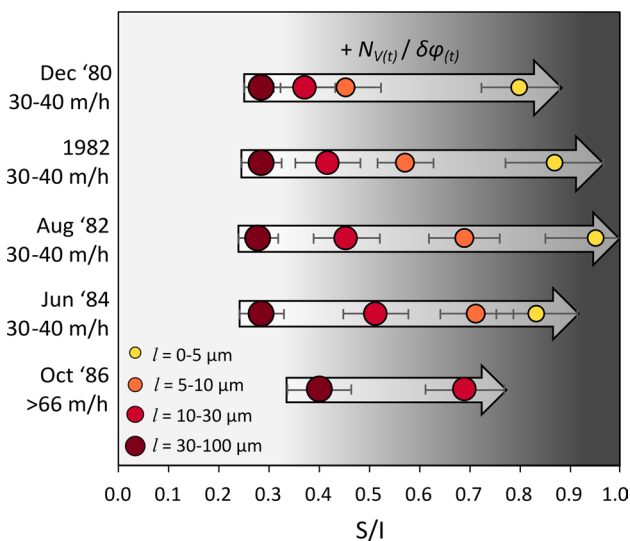


Fig. 10 Ranges of microlite shapes in dome rocks from the Mt. St. Helens 1980–86 eruption. Ascent rates are from Rutherford and Hill (1993). Larger S/l ranges represent wider nucleation intervals. See text for interpretation

of all plagioclase crystals in the magma and the crystallisation increment to be realised, i.e., $N_V / \Delta\phi$. High $N_V / \Delta\phi$ result in a low $\Delta V_{crystal}$ and produces final morphologies close to the original prismatic shape, whereas low $N_V / \Delta\phi$ results in high $\Delta V_{crystal}$ and will therefore change crystal shapes significantly. Our models also suggest that once crystals have reached ca. 20 μm in size, their morphology is unlikely to significantly change, at least in a scenario of decompression crystallisation of plagioclase microlites.

Thermodynamic considerations and the shape of plagioclase nuclei

Progressive overgrowth of micrometre-sized prismatic crystals by tabular shapes can explain the observed evolution of crystal shapes from rods to tablets as size increases. The shape endmembers chosen for the growth modelling reflect the range of shapes observed in natural silicic magmas (Fig. 4). Adjusting the shape of the overgrowing crystal will quantitatively affect the resulting shape distribution but will not change the pattern observed. However, little is yet known about the morphology of crystal nuclei—in any crystal phase, but particularly in multi-component silicate systems, due to the difficulties of direct observation at very small scales and because it is unknown whether bulk properties are relevant for nuclei. Classical nucleation theory (CNT) assumes a spherical nucleus shape since it was developed to describe phase changes in fluids (e.g., a bubble of vapour forming in a fluid). Crystal nucleation is also commonly described under the simplified assumption that crystal nuclei are spherical (e.g., Dowty 1980; Schmelzer et al. 2018). However, many crystals are anisotropic, with different faces having different interfacial free energies, and their minimum energy shape is therefore not spherical, but thought to reflect the interfacial free energies of respective faces (Gibbs–Curie–Wulff theorem; Gibbs 1876, 1878; Curie 1885; Wulff 1901; Herring 1951). Tolman (1949) further suggested that interfacial energies may be size-dependent, such that the equilibrium shape for crystal nuclei may not correspond to that of the macroscopic crystal. A fundamental assumption underlying these considerations is that crystal nuclei will assume the shape that minimises the free energy. However, De Yoreo and Vekilov (2003) suggest that only those nuclei that grow to critical sizes *fastest* will survive, and these shapes may deviate significantly from the shape that would minimise the interfacial free energy. This permits elongate nucleus shapes with high surface area to volume ratios (SA/V) and rough surfaces to be favoured over compact, smooth shapes (e.g. Gasser et al. 2001, reported in De Yoreo and Velikov 2003). In particular, both rods and tablets have higher SA/V than equant shapes, and for a given growth volume rods can achieve larger crystal sizes than tablets due to fast growth being concentrated on one dimension

only (e.g., $S:I:L=1:1:10$) rather than on two in the case of tablets (e.g., $1:10:10$).

Experimental evidence in other crystallising systems also supports preferred growth of elongate rods following crystal nucleation. For example, Shen et al. (2002) describe rapid anisotropic growth along the c crystallographic axis during nucleation of each of three Si_3N_4 -based ceramics: (trigonal α -sialon, hexagonal β -sialon, and orthorhombic O-sialon), forming prismatic crystals within minutes. Shen et al. (2002) call the process “dynamic [Ostwald] ripening” and suggest that local supersaturation in the liquid results in rapid precipitation “onto the crystallographic surfaces that will most easily accommodate” it (Shen et al. 2002). Similarly, Hammer and Rutherford (2002) describe growth of faceted, prismatic plagioclase crystals with $S \approx I$ in a Pinatubo dacite 20 min after single step decompression to $P_f=5\text{--}25$ MPa ($\Delta T_{\text{eff}}=186\text{--}266$ °C). Crucially, crystal shapes subsequently evolved towards tabular shapes with very low S/I as anneal time at P_f increased (Fig. 12 in Hammer and Rutherford 2002). This evolution is directly equivalent to the trend observed in the natural samples presented here, and it supports our interpretation that during decompression crystallisation, plagioclase may indeed nucleate preferentially as prismatic rods with high S/I , before growing the intermediate dimension to form tabular shapes with low S/I .

Application of the growth model to natural samples

In order to transfer these results to natural samples (i.e., volumes of magma), we first need to consider that crystallisation does not occur in discrete increments but as a continuous process. It is therefore useful to discard the static variables for total number density N_V , total (effective) undercooling ΔT_{eff} , and the crystallisation $\Delta\varphi$ required to minimise it. Instead, we introduce dynamic variables tracing the evolution of number density and undercooling during crystallisation: $N_{V(t)}$ is the cumulative number density and $\Delta T_{(t)}$ is the supersaturation of the magma at time t during crystallisation; $\delta\varphi_{(t)}$ is the crystallisation required to minimise $\Delta T_{(t)}$. Each of these variables is constantly changing as crystallisation proceeds. Assuming that nucleating plagioclase is prismatic with $S \approx I$, and that subsequent growth preferentially increases the intermediate dimension towards a tabular endmember (e.g., $I \approx L$), the shapes developed by individual plagioclase crystals can be predicted as a function of the available growth volume per crystal $\Delta V_{\text{crystal}}$, or $N_{V(t)}/\delta\varphi_{(t)}$ (Fig. 8a). For low $N_{V(t)}/\delta\varphi_{(t)}$, large growth volumes are available for individual crystals, hence they evolve into larger, tabular crystals. For high $N_{V(t)}/\delta\varphi_{(t)}$, on the other hand, $\Delta V_{\text{crystal}}$ is low, and individual crystals will grow less with little change in shape.

Crystallising magmas tend to evolve towards higher $N_{V(t)}/\delta\varphi_{(t)}$ as they nucleate and grow crystals, because $N_{V(t)}$

increases, which in turn facilitates a more effective reduction of $\Delta T_{(t)}$ and $\delta\varphi_{(t)}$ (Brandeis and Jaupart 1987; Hammer and Rutherford 2002). Tabular, low $N_{V(t)}/\delta\varphi_{(t)}$ shapes are therefore expected early during the crystallisation of a magma, and progressive nucleation will produce more prismatic, high $N_{V(t)}/\delta\varphi_{(t)}$ shapes towards the end of crystallisation (Fig. 8a). A similar evolution from disequilibrium to equilibrium shapes with increasing crystal number densities has been predicted by Lofgren (1974). The total range of S/I in a sample depends on (i) the number of pre-existing crystals $N_{V(t=0)}$ (e.g., the crystal cargo from magma reservoirs); and (ii) the specific cooling or decompression path, i.e. the temporal evolution of $\Delta T_{(t)}$, with $N_{V(t)}$ and $\delta\varphi_{(t)}$ being dependent on the nucleation rates imposed by $\Delta T_{(t)}$ (Hammer 2004). Specifically, the width of the nucleation interval exerts primary control over the variability of S/I in a sample: the growth model shows that crystal shape does not change after crystals have reached ca. 20 μm in size (Fig. 6), and therefore new generations of nuclei are required in order to trace the evolution of $N_{V(t)}/\delta\varphi_{(t)}$ in a magma. Slow decompression (Fig. 8b) or cooling favours nucleation over a wider interval and tends to produce a larger range of S/I in a sample than fast decompression (Fig. 8c) or cooling, where higher $\Delta T_{(t)}$ and $N_{V(t)}$ are achieved and crystallisation proceeds more rapidly (e.g., Hammer and Rutherford 2002; Hammer 2008; Riker et al. 2015). Different cooling and decompression paths and their effects on crystal textures have been extensively studied in decades of experiments in an effort to reproduce textures observed in natural samples (e.g., Lofgren 1974; Hammer and Rutherford 2002; Martel and Schmidt 2003; Martel 2012; Riker 2015; Befus and Andrews 2018; Lindoo and Cashman 2021). These works have highlighted stark differences in textural outcomes depending on the temporal evolution of $\Delta T_{(t)}$ (cf. Andrews and Befus 2020). Here, we illustrate the effect of varying ascent rates on crystal shapes using our dataset and model.

Firstly, we consider the Mt. St. Helens dome-building eruption between December 1980 and October 1986 (Figs. 8b, 9, 10). Experimental results (Geschwind and Rutherford 1995; Martel 2012) and other petrological constraints (Rutherford and Hill 1993) suggest that magma ascent was slow, with the exception of the initiation and end of the eruption. In this case, nucleation is quasi-continuous and in fact increasing during ascent, as evidenced by the generally increasing crystal numbers in successive fractions (Fig. 6a). This suggests that $\Delta T_{(t)}$ and $\delta\varphi_{(t)}$ tend to increase during ascent, likely due to degassing-induced increase of the liquidus and nucleation delays (Mollard et al. 2012; Rusiecka et al. 2020). The earliest plagioclase to nucleate deep in the conduit (Stage 1) crystallises at low $N_{V(t)}$, and resulting low $N_{V(t)}/\delta\varphi_{(t)}$ favours development of its tabular characteristic morphology (Fig. 9). These crystals subsequently continue to grow to be erupted as the $l=30\text{--}100$ μm

fraction. Further ascent and nucleation progressively escalates $N_{V(t)}$ of the magma (Stages 2–4), both due to increasing crystal numbers of individual fractions (Fig. 6a–c), and due to the cumulative effect of all crystal fractions in the magma (Fig. 6d–f). As a result, $N_{V(t)}/\delta\varphi_{(t)}$ rapidly increases, and subsequent crystal fractions have decreasing $\Delta V_{crystal}$ and develop increasingly higher S/I (Fig. 9). Meanwhile, the earliest crystals have grown to sizes large enough to prevent any further significant changes in shape. This illustrates how continuous nucleation and growth during slow ascent produce a large range in crystal shapes, with late-nucleating crystals retaining more prismatic shapes.

The time-series of the Mt. St. Helens dome-building eruption between December 1980 and October 1986 shows how variations in ascent rate may affect plagioclase microlite shapes (Fig. 10): the initial range of shapes of $S/I = 0.3$ – 0.8 in December 1980 increases to 0.3 – 1.0 in August 1982, with crystals $< 30 \mu\text{m}$ developing increasingly higher S/I shapes. This implies a widening nucleation interval due to generally slower ascent rates or longer stalling at shallow depth. A slight increase in ascent rates/shallow storage timescales is indicated by the smaller S/I range in the June 1984 sample. Ascent rates derived from amphibole breakdown rims (Rutherford and Hill 1993) do not show any significant variations during October 1980–84, but we note that these estimates are averaged, *minimum* timescales of ascent from the reservoir to the surface which may not fully describe the variability of complex ascent paths. By contrast, the sample for October 1986 lacks microlites $< 10 \mu\text{m}$, which suggests that storage at shallow depth was shorter than the nucleation delay of the magma, thereby suppressing nucleation entirely. This interpretation is consistent with amphibole breakdown timescales, which indicate significantly higher ascent rates for October 1986 (Rutherford and Hill 1993). Higher S/I for microlites $> 10 \mu\text{m}$ indicate slightly higher $N_{V(t)}/\delta\varphi_{(t)}$ (i.e., higher number densities) in the lower conduit, which may be due to a higher abundance of phenocrysts from the reservoir in this sample.

Secondly, textures distinct from our Mt. St. Helens dataset are observed for samples of the cryptodome (Cashman and Hoblitt 2004) and for pumice from eruptions in Summer 1980 (HND clasts; Cashman and McConnell 2005). These rocks are characterised by very high N_V , yet they are dominated by crystals $< 10 \mu\text{m}$ length with low to intermediate S/I , i.e., tablet shapes. Similar textures were observed in isolated pumice clasts at Pinatubo (P901; Hammer et al. 1999), as well as in sample AB22 from Galeras (Table 1; Fig. 8c; Bain et al. 2019). Such high- N_V textures are commonly interpreted to reflect rapid ascent and subsequent stalling at shallow depth (based on glass H_2O contents; Hammer et al. 1999; Cashman and Hoblitt 2004), possibly also involving mechanical breakage of crystals during

repressurisation (Lindoo and Cashman 2021). This scenario implies suppressed nucleation during most of the ascent path, followed by a single nucleation burst at shallow depth (Fig. 11). At the beginning of the nucleation burst, $\Delta T_{(t)}$ and $\delta\varphi_{(t)}$ approach total ΔT_{eff} and $\Delta\varphi$, which results in low $N_{V(t)}/\delta\varphi_{(t)}$ and high $\Delta V_{crystal}$. Our model therefore predicts tabular shapes for this scenario: Using a prismatic nucleus ($I = 0.5 \mu\text{m}$) and textural parameters for AB22 as input ($\Delta\varphi = 0.2$, $N_V = 8 \times 10^6 \text{mm}^{-3}$, Bain et al. 2019), our model yields a 3D shape of 1:5:8 (red circle in Fig. 8c), in agreement with the most tabular shapes of sample AB22. Furthermore, nucleation occurs over the narrow interval of the burst, rapidly driving down $\delta\varphi_{(t)}$, and as a result, the range of plagioclase shapes formed is much more restricted (Fig. 8c) than in the slow ascent case (Fig. 8b).

Implications for the relationship between undercooling, number density and crystal shape

The key concept of the model presented here is that the initial shapes of nucleating plagioclase crystals are metastable prisms, and that final microlite shapes are controlled by the growth volume available per crystal $\Delta V_{crystal}$, prescribed by the balance between crystal number density $N_{V(t)}$ and crystallisation potential $\delta\varphi_{(t)}$. The examples above illustrate that the temporal decompression (or cooling) *pathway* is the crucial parameter controlling groundmass textures (see also Andrews and Befus 2020). Hence, total number density N_V and total undercooling ΔT_{eff} are poor predictors of crystal shapes in a magma batch; instead, the temporal co-evolution of $\Delta T_{(t)}$ and $N_{V(t)}$ is key. A straightforward relationship between crystal shapes and ΔT_{eff} is therefore not to be expected. With this in mind, the established paradigm that higher undercoolings produce less equant crystals (e.g., Lofgren 1974; Walker et al. 1976; Kirkpatrick et al. 1979; Blundy and Cashman 2008; Shea and Hammer 2013) may not fully characterise crystal shape evolution during groundmass crystallisation of geological samples. In fact, assuming homogeneous nucleation, the *lowest* undercoolings are likely to produce low- S/I , tabular crystal shapes: nucleation rates strongly decrease with decreasing undercooling (Hammer 2004), hence low $\Delta T_{(t)}$ results in low $N_{V(t)}/\delta\varphi_{(t)}$, favouring growth of thin, tabular crystals. Indeed, the most elongated 2D plagioclase shapes reported by Hammer and Rutherford (2002) 20 min after single-step decompression ($\Delta T_{eff} \approx \Delta T_{(t)}$) are those crystallised in the experiments with the smallest decompression (i.e., lowest undercooling; $\Delta T_{eff} \leq 70\text{C}$, their Fig. 12). Similarly, single-step decompression experiments on a synthetic rhyodacite by Mollard et al. (2012) produced the lowest S/I for the lowest undercoolings ($\Delta T_{eff} = 55 \text{ }^\circ\text{C}$). In addition, as discussed above, any pre-existing crystals

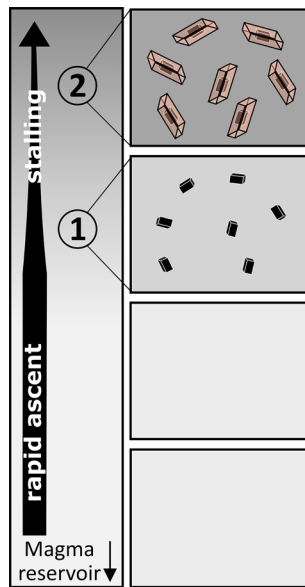


Fig. 11 Schematic for the textural evolution of intermediate magmas during rapid ascent and stalling at shallow depth. Nucleation is suppressed in the lower conduit as ascent is faster than the nucleation delay of plagioclase. Crystallisation occurs following a single nucleation burst at shallow depth (Stage 1–2); the lack of prior crystallisation imposes a large $\delta\varphi_{(t)}$ and therefore relatively high available growth volumes despite high number densities. Resulting textures are characterised by abundant, small, tabular crystals. See Fig. 8c for and text for further explanation

further modify $N_{V(t)}/\delta\varphi_{(t)}$ and therefore control numbers and shapes of growing crystals. We therefore conclude by stressing that the relationship between undercooling and shape is moderated by the specific crystallisation history of a magma.

Future work

Our model is based on natural and experimental samples with rhyolitic melt composition, which experienced moderate to high effective undercoolings in response to decompression. Lower effective undercoolings < 50 °C need to be studied to better understand and model magma reservoir processes. This is crucial because interfacial energies have been shown to vary as a function of ΔT_{eff} in decompression experiments (Hammer 2004), which may affect both nucleation and growth shapes. More generally, interfacial energies may vary with a number of parameters, including melt and crystal compositions (Takei and Shimizu 2003), melt viscosity and water contents (Hammer 2004; Mollard et al. 2020), and crystal size (Schmelzer et al. 2018). Variations in nucleus and overgrowth shapes as these parameters change are plausible and this needs to be explored and incorporated into the growth model. In particular, the model needs validation for basaltic compositions, where plagioclase crystals show

generally lower S/I shapes (i.e., thinner tablets; Fig. 8d). This may be partly explained by lower nucleation rates in less silicic melts (Shea and Hammer 2013) but could also be related to differences in plagioclase-melt interfacial energies due to lower melt viscosities. Moreover, experimental data for cooling experiments in basalts ($\Delta T/t = 1\text{--}60$ °C/h, total cooling of 19–500 °C; Pupier et al. 2008; Giuliani et al. 2020) show that some runs trace an offset from the trends observed in this study towards higher S/L (i.e., relative growth of S ; arrow in Fig. 8d). This second trend approximates what is commonly considered the Wulff shape for plagioclase. Plausible explanations for the relative increase of S include variations in diffusivities related to melt viscosity (Kitayama et al. 1998), different growth mechanisms at low undercoolings (e.g., Cabane et al. 2005), or synneusis (Pupier et al. 2008); more experiments are needed to explore this observation further.

Finally, more work is necessary on the effect of the temporal evolution of $N_{V(t)}$ and $\Delta T_{(t)}$ on crystal shapes. Suitable published experimental data may be complemented by new experiments constraining a variety of pre-existing crystals and temporal evolutions of $\Delta T_{(t)}$ to relate the range in crystal shapes in natural samples to specific undercooling histories, both in magma reservoirs (phenocrysts) and in the conduit (microlites). Crystal shape is an important factor controlling magma rheology (e.g., Mueller et al. 2010; Cimarelli et al. 2011; Moitra and Gonnermann 2015), which in turn affects mush unlocking timescales (Spera and Bohrsen 2018) and eruption styles (Bain et al. 2021; La Spina et al. 2021), hence a better understanding of how magma crystallisation pathways affect crystal shape is of crucial importance.

Conclusions

We studied variations in crystal shape as a function of size for plagioclase microlites ($l < 100$ μm) in intermediate magmas. The main findings of this work can be summarised as follows:

1. We present a new program to calculate 3D shapes from 2D crystal intersection data, *ShapeCalc* with improved range of model shapes, uncertainty estimation and precision. Stereological projections are based on the same models as those used in *CSDCorrections*, facilitating greater consistency in CSD analysis.
2. Crystal shape varies systematically with size in dome-forming magmas: the smallest crystals show prismatic 3D shapes ($S/I = 0.7\text{--}1$), whereas larger crystals generally have tabular habits ($S/I = 0.1\text{--}0.5$).
3. The trend from prismatic to tabular shapes with increasing crystal size reflects shape evolution during incipient

plagioclase growth, with nucleation as high- S/I prismatic rods and subsequent preferential overgrowth of the intermediate axis to form tabular shapes with low S/I .

4. Early-formed crystals grow to larger sizes and tabular shapes, whereas those formed late-stage tend to retain more prismatic habits.
5. Microlite crystal habits depend on the available growth volume per crystal, which is a function of the total number of crystals in the magma $N_{V(t)}$ at the time of nucleation, and the crystallisation volume $\delta\varphi(t)$ prescribed by the undercooling $\Delta T(t)$.
6. The total range of microlite shapes is controlled by the *temporal evolution* of undercooling and $N_{V(t)}$. In general, faster cooling/decompression produces a smaller range in crystal sizes and shapes than slow cooling/decompression. The proposed growth model can explain the range of textures observed in intermediate volcanic rocks with different ascent histories.
7. Variation in plagioclase crystal shapes is of petrogenetic significance and an important factor to consider when constructing CSDs and using fluid dynamical models involving magma rheology.

Supplementary Information The online version contains supplementary material available at <https://doi.org/10.1007/s00410-022-01922-9>.

Acknowledgements We thank Kari Cooper for providing the Mt. St. Helens samples, Leon Bowen of the GJ Russell Electron Microscopy Facility at Durham University for facilitating data acquisition, and Amelia Bain for sharing the textural data for Galeras rocks. We further thank the editor and an anonymous reviewer for their constructive reviews, as well as Heather Wright for insightful feedback that helped improve the manuscript. This work was funded by UK Natural Environment Research Council grant NE/T000430/1.

Open Access This article is licensed under a Creative Commons Attribution 4.0 International License, which permits use, sharing, adaptation, distribution and reproduction in any medium or format, as long as you give appropriate credit to the original author(s) and the source, provide a link to the Creative Commons licence, and indicate if changes were made. The images or other third party material in this article are included in the article's Creative Commons licence, unless indicated otherwise in a credit line to the material. If material is not included in the article's Creative Commons licence and your intended use is not permitted by statutory regulation or exceeds the permitted use, you will need to obtain permission directly from the copyright holder. To view a copy of this licence, visit <http://creativecommons.org/licenses/by/4.0/>.

References

- Andrews BJ, Befus KS (2020) Supersaturation nucleation and growth of plagioclase: a numerical model of decompression-induced crystallization. *Contrib Mineral Petrol* 175(3):1–20. <https://doi.org/10.1007/s00410-020-1660-9>
- Bain AA, Calder ES, Cortés JA, Cortés GP, Loughlin SC (2019) Textural and geochemical constraints on andesitic plug emplacement prior to the 2004–2010 vulcanian explosions at Galeras volcano. *Colombia Bull Volcanol* 81(1):1–25. <https://doi.org/10.1007/s00445-018-1260-y>
- Bain AA, Kendrick JE, Lamur A, Lavallée Y, Calder ES, Cortés JA, Cortés GP, Gómez Martínez D, Torres RA (2021) Micro-textural controls on magma rheology and Vulcanian explosion cyclicality. *Front Earth Sci* 8:703. <https://doi.org/10.3389/feart.2020.611320>
- Befus KS, Andrews BJ (2018) Crystal nucleation and growth produced by continuous decompression of Pinatubo magma. *Contrib Mineral Petrol* 173(11):1–20. <https://doi.org/10.1007/s00410-018-1519-5>
- Blundy J, Cashman K (2008) Petrologic reconstruction of magmatic system variables and processes. *Rev Mineral Geochem* 69(1):179–239. <https://doi.org/10.2138/rmg.2008.69.6>
- Brandeis G, Jaupart C (1987) The kinetics of nucleation and crystal growth and scaling laws for magmatic crystallization. *Contrib Mineral Petrol* 96(1):24–34
- Brugger CR, Hammer JE (2010) Crystallization kinetics in continuous decompression experiments: implications for interpreting natural magma ascent processes. *J Petrol* 51(9):1941–1965. <https://doi.org/10.1093/petrology/egq044>
- Cabane H, Laporte D, Provost A (2005) An experimental study of Ostwald ripening of olivine and plagioclase in silicate melts: implications for the growth and size of crystals in magmas. *Contrib Mineral Petrol* 150(1):37–53. <https://doi.org/10.1007/s00410-005-0002-2>
- Cashman KV (2020) Crystal size distribution (CSD) analysis of volcanic samples: advances and challenges. *Front Earth Sci* 8:1–17. <https://doi.org/10.3389/feart.2020.00291>
- Cashman KV, Hoblitt RP (2004) Magmatic precursors to the 18 May 1980 eruption of Mount St. Helens USA. *Geology*. <https://doi.org/10.1130/g20078.1>
- Cashman KV, Marsh BD (1988) Crystal size distribution (CSD) in rocks and the kinetics and dynamics of crystallization II: Makaopuhi lava lake. *Contrib Mineral Petrol* 99(3):292–305. <https://doi.org/10.1007/BF00375363>
- Cashman K, McConnell S (2005) Multiple levels of magma storage during the 1980 summer eruptions of Mount St. Helens WA. *Bull Volcanol* 68(1):57–75. <https://doi.org/10.1007/s00445-005-0422-x>
- Cimarelli C, Costa A, Mueller S, Mader HM (2011) Rheology of magmas with bimodal crystal size and shape distributions: insights from analog experiments. *Geochem Geophys Geosyst*. <https://doi.org/10.1029/2011GC003606>
- Cooper KM, Donnelly CT, Sherrod DR, Scott WE, Stauffer PH (2008) 238U-230Th-226Ra Disequilibria in Dacite and Plagioclase from the 2004–2005 Eruption of Mount St. Helens. 827–846 doi:<https://doi.org/10.3133/pp175036>
- Couch S, Harford C, Sparks R, Carroll M (2003) Experimental constraints on the conditions of formation of highly calcic plagioclase microlites at the Soufrière Hills Volcano Montserrat. *J Petrol* 44(8):1455–1475. <https://doi.org/10.1093/petrology/44.8.1455>
- Curie P (1885) Sur la formation des cristaux et sur les constantes capillaires de leurs différentes faces. *Bull Mineral* 8(6):145–150
- De Yoreo JJ, Vekilov PG (2003) Principles of crystal nucleation and growth. *Rev Mineral Geochem* 54(1):57–93. <https://doi.org/10.2113/0540057>
- Dowty E (1980) Crystal growth and nucleation theory and the numerical simulation of igneous crystallization. Princeton University Press, In *Physics of magmatic processes*, pp 419–486
- Duchêne S, Pupier E, De Veslud CLC, Toplis MJ (2008) A 3D reconstruction of plagioclase crystals in a synthetic basalt. *Am Mineral* 93(5–6):893–901. <https://doi.org/10.2138/am.2008.2679>

- Gasser U, Weeks ER, Schofield A, Pusey P, Weitz D (2001) Real-space imaging of nucleation and growth in colloidal crystallization. *Science* 292(5515):258–262. <https://doi.org/10.1126/science.1058457>
- Geschwind C-H, Rutherford MJ (1995) Crystallization of microlites during magma ascent: the fluid mechanics of 1980–1986 eruptions at Mount St Helens. *Bull Volcanol* 57(5):356–370. <https://doi.org/10.1007/BF00301293>
- Gibbs JW (1878) On the equilibrium of heterogeneous substances. *Am J Sci* 3(96):441–458
- Gibbs J (1876) On the equilibrium of heterogeneous substances, vol. 1. In, vol. Longmans, Green, and Co., New York,
- Giuliani L, Iezzi G, Vetere F, Behrens H, Mollo S, Cauti F, Ventura G, Scarlato P (2020) Evolution of textures, crystal size distributions and growth rates of plagioclase, clinopyroxene and spinel crystallized at variable cooling rates from a mid-ocean ridge basaltic melt. *Earth Sci Rev*. <https://doi.org/10.1016/j.earscirev.2020.103165>
- Hammer JE (2004) Crystal nucleation in hydrous rhyolite: experimental data applied to classical theory. *Am Mineral* 89(11–12):1673–1679. <https://doi.org/10.2138/am-2004-11-1212>
- Hammer JE (2008) Experimental studies of the kinetics and energetics of magma crystallization. *Rev Mineral Geochem* 69(1):9–59. <https://doi.org/10.2138/rmg.2008.69.2>
- Hammer JE, Rutherford MJ (2002) An experimental study of the kinetics of decompression-induced crystallization in silicic melt. *J Geophys Res Solid Earth*. <https://doi.org/10.1029/2001jb000281>
- Herring C (1951) Some theorems on the free energies of crystal surfaces. *Phys Rev* 82(1):87
- Higgins MD (1994) Numerical modeling of crystal shapes in thin sections: estimation of crystal habit and true size. *Am Mineral* 79(1–2):113–119
- Higgins MD (2000) Measurement of crystal size distributions. *Am Mineral* 85(9):1105–1116. <https://doi.org/10.2138/am-2000-8-901>
- Higgins MD (2006) Quantitative textural measurements in igneous and metamorphic petrology. Cambridge University Press
- Higgins MD, Chandrasekharam D (2007) Nature of sub-volcanic magma chambers, Deccan Province, India: evidence from quantitative textural analysis of plagioclase megacrysts in the Giant Plagioclase Basalts. *J Petrol* 48(5):885–900. <https://doi.org/10.1093/ptrology/egm005>
- Iezzi G, Mollo S, Torresi G, Ventura G, Cavallo A, Scarlato P (2011) Experimental solidification of an andesitic melt by cooling. *Chem Geol* 283(3–4):261–273. <https://doi.org/10.1016/j.chemgeo.2011.01.024>
- Kirkpatrick RJ (1975) Crystal growth from the melt: a review. *Am Mineral J Earth Planet Mater* 60(9–10):798–814
- Kirkpatrick RJ, Klein L, Uhlmann DR, Hays JF (1979) Rates and processes of crystal growth in the system anorthite-albite. *J Geophys Res Solid Earth* 84(B7):3671–3676. <https://doi.org/10.1029/JB084iB07p03671>
- Kitayama M, Hirao K, Toriyama M, Kanzaki S (1998) Modeling and simulation of grain growth in Si₃N₄—I Anisotropic Ostwald Ripening. *Acta Mater* 46(18):6541–6550. [https://doi.org/10.1016/S1359-6454\(98\)00290-0](https://doi.org/10.1016/S1359-6454(98)00290-0)
- Kostov I, Kostov R (1999) Crystal habits of minerals. Bulgarian Academic Monographs (1). Prof Marin Drinov Academic Publishing House & Pensoft Publishers
- La Spina G, Arzilli F, Llewellyn E, Burton M, Clarke AB, Vitturi MdM, Polacci M, Hartley M, Di Genova D, Mader H (2021) Explosivity of basaltic lava fountains is controlled by magma rheology, ascent rate and outgassing. *Earth Planet Sci Lett* 553:116658. <https://doi.org/10.1016/j.epsl.2020.116658>
- Lindoo A, Cashman KV (2021) High crystal number densities from mechanical damage. *Front Earth Sci* 9:318. <https://doi.org/10.3389/feart.2021.659459>
- Lofgren G (1974) An experimental study of plagioclase crystal morphology; isothermal crystallization. *Am J Sci* 274(3):243–273. <https://doi.org/10.2475/ajs.274.3.243>
- Lofgren GE, Donaldson CH, Williams RJ, Mullins O Jr, Usselman TM (1974) Experimentally reproduced textures and mineral chemistry of Apollo 15 quartz normative basalts. Pergamon Press, Oxford
- Lormand C, Zellmer GF, Németh K, Kilgour G, Mead S, Palmer AS, Sakamoto N, Yurimoto H, Moebis A (2018) Weka trainable segmentation plugin in imagej: a semi-automatic tool applied to crystal size distributions of microlites in volcanic rocks. *Microsc Microanal* 24(6):667–675. <https://doi.org/10.1017/S1431927618015428>
- Lormand C, Zellmer GF, Kilgour G, Nemeth K, Palmer AS, Sakamoto N, Yurimoto H, Kuritani T, Iizuka Y, Moebis A (2020) Slow ascent of unusually hot intermediate magmas triggering Strombolian to sub-Plinian eruptions. *J Petrol*. <https://doi.org/10.1093/ptrology/egaa077>
- Marsh BD (1988) Crystal size distribution (CSD) in rocks and the kinetics and dynamics of crystallization. *Contrib Mineral Petrol* 99(3):277–291. <https://doi.org/10.1007/bf00375362>
- Martel C (2012) Eruption dynamics inferred from microlite crystallization experiments: application to Plinian and dome-forming eruptions of Mt. Pelée (Martinique, Lesser Antilles). *J Petrol* 53(4):699–725
- Martel C, Poussineau S (2007) Diversity of eruptive styles inferred from the microlites of Mt Pelée andesite (Martinique, Lesser Antilles). *J Volcanol Geotherm Res* 166(3–4):233–254. <https://doi.org/10.1016/j.jvolgeores.2007.08.003>
- Martel C, Schmidt BC (2003) Decompression experiments as an insight into ascent rates of silicic magmas. *Contrib Mineral Petrol* 144(4):397–415. <https://doi.org/10.1007/s00410-002-0404-3>
- Mock A, Jerram D (2005) Crystal size distributions (CSD) in three dimensions: insights from the 3D reconstruction of a highly porphyritic rhyolite. *J Petrol* 46(8):1525–1541. <https://doi.org/10.1093/ptrology/egi024>
- Moitra P, Gonnermann H (2015) Effects of crystal shape-and size-modality on magma rheology. *Geochem Geophys Geosyst* 16(1):1–26. <https://doi.org/10.1002/2014GC005554>
- Mollard E, Martel C, Bourdier J-L (2012) Decompression-induced crystallization in hydrated silica-rich melts: empirical models of experimental plagioclase nucleation and growth kinetics. *J Petrol* 53(8):1743–1766. <https://doi.org/10.1093/ptrology/egs031>
- Mollard E, Martel C, Le Trong E, Rogerie G (2020) Theoretical models of decompression-induced plagioclase nucleation and growth in hydrated silica-rich melts. *Front Earth Sci* 8:203. <https://doi.org/10.3389/feart.2020.00203>
- Morgan DJ, Jerram DA (2006) On estimating crystal shape for crystal size distribution analysis. *J Volcanol Geotherm Res* 154(1–2):1–7. <https://doi.org/10.1016/j.jvolgeores.2005.09.016>
- Morgan DJ, Jerram DA, Chertkoff DG, Davidson JP, Pearson DG, Kronz A, Nowell GM (2007) Combining CSD and isotopic microanalysis: magma supply and mixing processes at Stromboli Volcano, Aeolian Islands Italy. *Earth Planet Sci Lett* 260(3–4):419–431. <https://doi.org/10.1016/j.epsl.2007.05.037>
- Mueller S, Llewellyn E, Mader H (2010) The rheology of suspensions of solid particles. *Proc R Soc A Math Phys Eng Sci* 466(2116):1201–1228. <https://doi.org/10.1098/rspa.2009.0445>
- Muncill GE, Lasaga AC (1987) Crystal-growth kinetics of plagioclase in igneous systems; one-atmosphere experiments and application of a simplified growth model. *Am Mineral* 72(3–4):299–311
- Muncill GE, Lasaga AC (1988) Crystal-growth kinetics of plagioclase in igneous systems; isothermal H₂O-saturated experiments and extension of a growth model to complex silicate melts. *Am Mineral* 73(9–10):982–992
- Murch AP, Cole PD (2019) Using microlites to gain insights into ascent conditions of differing styles of volcanism at Soufrière

- Hills Volcano. *J Volcanol Geotherm Res* 384:221–231. <https://doi.org/10.1016/j.jvolgeores.2019.07.022>
- Nabelek PI, Taylor LA, Lofgren GE (1978) Nucleation and growth of plagioclase and the development of textures in a high-alumina basaltic melt. In: Proceedings of the Ninth Lunar and Planetary Science Conference, Houston, Texas, March 13–17, 1978, vol. Pergamon Press,
- Preece K, Barclay J, Gertisser R, Herd RA (2013) Textural and micro-petrological variations in the eruptive products of the 2006 dome-forming eruption of Merapi volcano, Indonesia: implications for sub-surface processes. *J Volcanol Geotherm Res* 261:98–120. <https://doi.org/10.1016/j.jvolgeores.2013.02.006>
- Preece K, Gertisser R, Barclay J, Charbonnier SJ, Komorowski J-C, Herd RA (2016) Transitions between explosive and effusive phases during the cataclysmic 2010 eruption of Merapi volcano, Java Indonesia. *Bull Volcanol* 78(8):1–16. <https://doi.org/10.1007/s00445-016-1046-z>
- Pupier E, Duchene S, Toplis MJ (2008) Experimental quantification of plagioclase crystal size distribution during cooling of a basaltic liquid. *Contrib Mineral Petrol* 155(5):555–570. <https://doi.org/10.1007/s00410-007-0258-9>
- Riker JM, Cashman KV, Rust AC, Blundy JD (2015) Experimental constraints on plagioclase crystallization during H₂O- and H₂O–CO₂-saturated magma decompression. *J Petrol* 56(10):1967–1998. <https://doi.org/10.1093/petrology/egv059>
- Rusiecka MK, Bilodeau M, Baker DR (2020) Quantification of nucleation delay in magmatic systems: experimental and theoretical approach. *Contrib Mineral Petrol* 175(5):1–16. <https://doi.org/10.1007/s00410-020-01682-4>
- Rutherford MJ, Hill PM (1993) Magma ascent rates from amphibole breakdown: an experimental study applied to the 1980–1986 Mount St. Helens eruptions. *J Geophys Res Solid Earth*. <https://doi.org/10.1029/93JB01613>
- Salisbury MJ, Bohron WA, Clyne MA, Ramos FC, Hoskin P (2008) Multiple plagioclase crystal populations identified by crystal size distribution and in situ chemical data: implications for timescales of magma chamber processes associated with the 1915 eruption of Lassen Peak, CA. *J Petrol* 49(10):1755–1780. <https://doi.org/10.1093/petrology/egn045>
- Schmelzer JW, Abyzov AS, Ferreira EB, Fokin VM (2018) Curvature dependence of the surface tension and crystal nucleation in liquids. *Int J Appl Glas Sci* 10(1):57–68. <https://doi.org/10.1111/ijag.12900>
- Schneider CA, Rasband WS, Eliceiri KW (2012) NIH Image to ImageJ: 25 years of image analysis. *Nat Methods* 9(7):671–675. <https://doi.org/10.1038/nmeth.2089>
- Scott JA, Mather TA, Pyle DM, Rose WI, Chigna G (2012) The magmatic plumbing system beneath Santiaguito Volcano, Guatemala. *J Volcanol Geotherm Res* 237:54–68. <https://doi.org/10.1016/j.jvolgeores.2012.05.014>
- Scott JA, Pyle DM, Mather TA, Rose WI (2013) Geochemistry and evolution of the Santiaguito volcanic dome complex, Guatemala. *J Volcanol Geotherm Res* 252:92–107. <https://doi.org/10.1016/j.jvolgeores.2012.11.011>
- Shea T, Hammer JE (2013) Kinetics of cooling- and decompression-induced crystallization in hydrous mafic-intermediate magmas. *J Volcanol Geotherm Res* 260:127–145. <https://doi.org/10.1016/j.jvolgeores.2013.04.018>
- Shen Z, Zhao Z, Peng H, Nygren M (2002) Formation of tough interlocking microstructures in silicon nitride ceramics by dynamic ripening. *Nature* 417(6886):266–269. <https://doi.org/10.1038/417266a>
- Spera FJ, Bohron WA (2018) Rejuvenation of crustal magma mush: a tale of multiply nested processes and timescales. *Am J Sci* 318(1):90–140. <https://doi.org/10.2475/01.2018.05>
- Streck MJ, Broderick CA, Thornber CR, Clyne MA, Pallister JS (2008) Plagioclase populations and zoning in dacite of the 2004–2005 Mount St. Helens eruption: constraints for magma origin and dynamics. US Geological Survey Professional Paper 1750 doi:<https://doi.org/10.3133/pp175034>
- Takei Y, Shimizu I (2003) The effects of liquid composition, temperature, and pressure on the equilibrium dihedral angles of binary solid–liquid systems inferred from a lattice-like model. *Phys Earth Planet Inter* 139(3–4):225–242. <https://doi.org/10.1016/j.pepi.2003.08.004>
- Tolman RC (1949) The effect of droplet size on surface tension. *J Chem Phys* 17(3):333–337
- Walker D, Kirkpatrick RJ, Longhi J, Hays JF (1976) Crystallization history of lunar picritic basalt sample 12002: phase-equilibria and cooling-rate studies. *Geol Soc Am Bull*. <https://doi.org/10.1130/0016-7606>
- Wallace PA, Lamb OD, De Angelis S, Kendrick JE, Hornby AJ, Díaz-Moreno A, González PJ, von Aulock FW, Lamur A, Utley JE (2020) Integrated constraints on explosive eruption intensification at Santiaguito dome complex, Guatemala. *Earth Planet Sci Lett*. <https://doi.org/10.1016/j.epsl.2020.116139>
- Watanabe K, Kitamura M (1992) Growth mechanisms of plagioclase in a basaltic melt. *Mineral J* 16(4):201–214. <https://doi.org/10.2465/minerj.16.201>
- Wulff G (1901) Xxv. zur frage der geschwindigkeit des wachstums und der auflösung der krystallflächen. *Zeitschrift für Kristallographie-Crystalline. Materials* 34(1–6):449–530

Publisher's Note Springer Nature remains neutral with regard to jurisdictional claims in published maps and institutional affiliations.